The Diversity of Extremely Red Objects

Ian Smail – University of Durham
F. N. Owen – National Radio Astronomy Observatory
G. E. Morrison – California Institute of Technology
William C. Keel – University of Alabama
R. J. Ivison – Royal Observatory
M. J. Ledlow – Gemini Observatory

Citation of published version:

Smail, I., Owen, F., Morrison, G., Keel, W., Ivison, R., Ledlow, M. (2002): The Diversity of Extremely Red Objects. *The Astrophysical Journal*, 581(2). DOI: https://doi.org/10.1086/344440

The Astrophysical Journal, 581:844–864, 2002 December 20

THE DIVERSITY OF EXTREMELY RED OBJECTS

Ian Smail,[1,2] F. N. Owen,[2,3] G. E. Morrison,[2,4] W. C. Keel,[2,5] R. J. Ivison,[6] and M. J. Ledlow[2,7]

Received 2002 May 7; accepted 2002 August 27

ABSTRACT

We present the results from a sensitive multiwavelength analysis of the properties of extremely red objects (EROs). Our analysis employs deep *RIzJHK* photometry of an $8\farcm5 \times 8\farcm5$ region to select a sample of 68 EROs with $(R-K) \geq 5.3$ and brighter than $K = 20.5$ ($5\,\sigma$). We combine this photometric data set with an extremely deep 1.4 GHz radio map of the field obtained from the VLA. This map reaches a $1\,\sigma$ limiting flux density of 3.5 μJy, making it the deepest 1.4 GHz map taken, and is sensitive enough to detect an active galaxy with $L_{1.4} \gtrsim 10^{23}$ W Hz^{-1} at $z > 1$. If powered by a starburst, this radio luminosity is equivalent to a star formation rate of $\gtrsim 25\ M_\odot$ yr^{-1} for stars more massive than $5\ M_\odot$. We identify radio counterparts to 21 of the EROs in this field with radio fluxes above 12.6 μJy and resolve one-third of these with our $1\farcs6$ FWHM beam. The spectral energy distributions of the majority of these galaxies are consistent with those expected for dust-reddened starbursts at $z \sim 1$. At these redshifts the radio luminosities of these galaxies indicate a median far-infrared luminosity of this population of $L_{\rm FIR} \gtrsim 10^{12}\ L_\odot$, meaning that half of the radio-detected sample are ultraluminous infrared galaxies (ULIRGs). We conclude that $\gtrsim 16\% \pm 5\%$ of the ERO population brighter than $K = 20.5$ are luminous infrared galaxies (LIRGs) at $z \sim 1$. We also use photometric classification of the colors of the EROs to investigate the mix of dusty active and evolved passive systems in the remaining ERO population that is undetected in our radio map. Based on this we suggest that at least 30% and possibly up to $\sim$60% of *all* EROs with $(R-K) \geq 5.3$ and $K \leq 20.5$ are dusty, star-forming systems at $z \gtrsim 1$. Our best estimate of the star formation density in this highly obscured and optically faint ($R \gtrsim 26$) population is $\dot{\rho}_*(0.1\text{–}100\ M_\odot) = 0.11 \pm 0.03\ M_\odot$ yr^{-1} Mpc^{-3}, comparable to estimates of that in Hα-emitting galaxies at $z \sim 1$ and greater than the estimates from UV-selected samples at these epochs. This lends support to the claims of a strong increase in the contribution from obscured systems to the star formation density at high redshifts. Using the observed counts of the radio-detected ERO population, we model the apparent break in the *K*-band number counts of the whole ERO population at $K \sim 19\text{–}20$ and propose that the passive ERO class dominates the total population in a relatively narrow magnitude range around $K \lesssim 20$, with dusty, active EROs making up the bulk of the population at fainter limits.

Subject headings: cosmology: observations — galaxies: clusters: individual (A851, Cl 0939+4713) — galaxies: evolution — galaxies: starburst — infrared: galaxies

1. INTRODUCTION

The last five years have seen a growing appreciation of the diversity of galaxy properties at $z \gtrsim 1\text{–}3$. In part this has arisen from an impressive improvement in the quality of the observations of galaxies at these redshifts, driven by the availability of powerful new instruments on 8 m class telescopes (e.g., NIRSPEC on Keck and ISAAC on the VLT). However, an equal role has been played by the realization of the necessity of a multiwavelength approach to studies of galaxy evolution at $z \gtrsim 1$. Thus, a range of new surveys spanning wave bands from the X-ray, near- and mid-infrared, submillimeter, and out to the radio have complimented the traditional view of distant galaxies based on UV/optical observations. These new studies have all tended to stress the role of dust obscuration in censoring our view of the galaxy population at high redshifts and especially in disguising the extent of activity in the most luminous systems, both AGN and star-forming. Indeed, our current, incomplete knowledge of the evolution of dusty galaxies suggests that some of the most active galaxies in the distant universe may be so obscured as to be undetectable in even the most sensitive UV/optical observations (e.g., Haarsma et al. 2000; Smail et al. 2002a).

One central theme to appear from this new multiwavelength view of galaxy formation is the ubiquity of optically faint, but bright near-infrared, counterparts to sources identified in many wave bands: the X-ray (Alexander et al. 2001, 2002; Cowie et al. 2001; Page et al. 2002; Stevens et al. 2002; Mainieri et al. 2002), the mid-infrared (Pierre et al. 2001; Smith et al. 2001; Franceschini et al. 2002), submillimeter (Smail et al. 1999a; Lutz et al. 2001; Ivison et al. 2002), and radio bands (Richards et al. 1999; Chapman et al. 2001). This has resulted in a renaissance in interest in such extremely red objects (EROs), a class of galaxies that had previously been viewed as a curiosity with little relevance to our understanding of galaxy formation and evolution, comprising as they do a mere $\sim$5%–10% of the population at $K \leq 20$.

The ERO class is photometrically defined: the most frequently used definition is now $(R-K) \geq 5.3$. This very red

[1] Institute for Computational Cosmology, University of Durham, South Road, Durham DH1 3LE, UK.
[2] Visiting Astronomer, Kitt Peak National Observatory, National Optical Astronomy Observatory, operated by AURA, Inc., under cooperative agreement with the National Science Foundation.
[3] National Radio Astronomy Observatory, P.O. Box O, Socorro, NM 87801.
[4] California Institute of Technology, Infrared Processing and Analysis Center, MS 100-22, Pasadena, CA 91125.
[5] Department of Physics and Astronomy, University of Alabama, Box 870324, 206 Gallalee Hall, Tuscaloosa, AL 35487.
[6] Astronomy Technology Centre, Royal Observatory, Blackford Hill, Edinburgh EH9 3HJ, UK.
[7] Gemini Observatory, Southern Operations Center, Association of Universities for Research in Astronomy, Casilla 603, La Serena, Chile.

optical/near-infrared color is intended to isolate two broad populations of galaxies at $z \gtrsim 1$: those that are red by virtue of the presence of large amounts of dust (resulting from active star formation), as well as passive systems whose red colors arise from the dominance of old, evolved stars in their stellar populations. The very different natures of these two subclasses have prompted efforts to disentangle their relative contributions to the ERO population (Pozzetti & Mannucci 2000; Mannucci et al. 2002) so that well-defined samples can be used to test galaxy formation models (Daddi et al. 2000; Smith et al. 2002b; Firth et al. 2002).

Studies of the ERO population have turned up hints of the diverse nature of this population, including an apparent break in the number counts of EROs at $K \sim 19$–20 (McCarthy et al. 2001; Smith et al. 2002b). This feature is roughly 2 mag fainter than the well-known break in the total K-band counts of the faint field population (Gardner, Cowie, & Wainscoat 1993). The cumulative count slope of EROs [$\log_{10} N(< K) \propto \alpha K$] drops from $\alpha = 0.81 \pm 0.05$ at bright magnitudes to $\alpha = 0.32 \pm 0.05$ for the fainter EROs (e.g., Smith et al. 2002b; Chen et al. 2002). This break in the counts either could result from a relatively narrow redshift range probed by the selection criteria of EROs (with the change in the integrated counts then being simply related to the form of the luminosity function of the ERO population) or may reflect differing evolutionary behavior in subpopulations, where one class of EROs declines rapidly beyond $K \sim 19$. To test this suggestion, we need to track the relative mix of galaxy types within the ERO population to $K > 19$–20.

Techniques to separate the passive, evolved and obscured, active populations include near-infrared photometric classifications (Pozzetti & Mannucci 2000; Smith et al. 2002b; Mannucci et al. 2002), submillimeter emission (Dey et al. 1999; Mohan et al. 2002), X-ray emission (Alexander et al. 2001, 2002; Brusa et al. 2002), and optical/near-infrared spectroscopy (Cimatti et al. 2002; Smith et al. 2001, 2002a). Of these approaches, by far the largest and most influential project is the "K20" survey undertaken by Cimatti et al. (2002), who obtained spectroscopic classifications for 29 EROs with $K < 19.2$ and $(R-K) \geq 5$ from a full sample of 45. The median redshift of their $K < 19.2$ sample is $z = 1.1 \pm 0.2$, with galaxies spread across $z = 0.7$–1.4 (see Daddi et al. 2001), and they find that their sample is split equally into passive, evolved and active, dusty EROs: 31%–64% versus 67%–33%, where the ranges reflect the uncertainty due to the incompleteness in their survey. The K20 survey has significantly increased our knowledge of the ERO population; however, it is reliant on identifying emission lines in the rest-frame UV spectra of possibly dusty galaxies, which results in an incomplete and perhaps biased view of the mix of galaxies within the population. Moreover, the magnitude limit achieved for the high-completeness sample, $K < 19.2$, means that it cannot be used to track the variation in the properties of the population across the break in the counts of EROs.

Here we apply a new technique to investigate the mix of the ERO population at faint magnitudes: using very deep radio observations at 1.4 GHz, which are both sensitive enough to identify strongly star-forming galaxies out to high redshifts, $z \gtrsim 1$–2, and yet insensitive to the effects of dust obscuration (Mohan et al. 2002; Chapman et al. 2002b). Radio surveys to submillijansky flux limits have shown the usefulness of this technique for identifying star-forming galaxies in the distant universe: morphological classifications from *Hubble Space Telescope* (*HST*) imaging show that many are blue disk galaxies (Windhorst et al. 1994; Richards et al. 1998; Richards 2000), with optical spectroscopy confirming that these are apparently normal star-forming galaxies at intermediate redshifts (Benn et al. 1993; Mobasher et al. 1999; Roche, Lowenthal, & Koo 2002b), with a small proportion of AGNs (20% based on their radio morphologies in very high resolution maps from combined VLA and Merlin observations [Muxlow et al. 1999], with most of these having blue colors). However, the spectral properties of the galaxies in these surveys also show signatures of the presence of dust, which may be cloaking the strength of the activity in these systems and making them appear more mundane than they should (Hammer et al. 1995; Poggianti & Wu 2000; Smail et al. 1999b).

More recently, samples of faint radio sources have begun to be used to attempt to identify obscured star-forming galaxies at even higher redshifts. By focusing on those radio sources with faint or undetectable counterparts in the optical, these surveys attempt to isolate the most distant star-forming galaxies in the radio samples (Richards et al. 1999; Barger, Cowie, & Richards 2000; Chapman et al. 2001, 2002b). Sensitive submillimeter observations of these optically faint radio sources confirm that a large fraction of them are luminous, dusty systems at redshifts of $z \sim 1$–3, although, as with the whole submillimeter galaxy population, there is still considerable uncertainty over their exact redshifts (Chapman et al. 2002a). The relationship between these highly obscured but very luminous galaxies and the perhaps less-obscured systems selected through Lyα emission and the Lyman break technique is a crucial issue for a complete understanding of the formation and evolution of galaxies (Smail et al. 2002a, 2002b). The project described here seeks to trace the population of the luminous, dusty galaxies detected in the submillimeter at $z \gtrsim 2$ to lower redshifts and lower luminosities. These samples should be more amenable to detailed study and so provide a clearer connection between the evolution of the obscured and unobscured galaxies over the lifetime of the universe (Chapman et al. 2002a).

In this paper we use an extremely deep VLA radio map to investigate the radio emission from a sample of ERO galaxies at a sensitivity limit sufficient to detect strongly star-forming galaxies at $z \gtrsim 1$–2. We also present extensive optical/near-infrared imaging of this ERO sample. We exploit this deep *RIzJHK* photometry to analyze the spectral energy distributions (SEDs) of the EROs and investigate their properties in detail. We present our observations, their reduction, and cataloging in the next section, describe our analysis and results in § 3, and discuss these in § 4 before giving our conclusions in § 5. Throughout we assume a cosmological model with $q_0 = 0.5$ and $H_0 = 50$ km s^{-1} Mpc^{-1}. If we instead adopted the currently fashionable $H_0 = 70$ km s^{-1} Mpc^{-1}, $\Omega_\Lambda = 0.7$, $\Omega_m = 0.3$ cosmology, then for a source at $z = 1$ all the linear sizes we derive would be 6% smaller, the luminosities would be 10% fainter, and the volume densities would be 10% lower.

2. OBSERVATIONS, REDUCTION, AND CATALOGING

The field used for our analysis contains the $z = 0.41$ cluster A851 (Cl 0939+4713). This well-studied cluster is relatively rich but very irregular in appearance (Dressler et

al. 1994, 1997; A. Dressler et al. 2002, in preparation; Iye et al. 2001; Schindler et al. 1998). As we discuss below, although cluster members may contribute significantly to the optically bright radio population in this field, the extremely red radio sources discussed in this work all probably lie at $z \gtrsim 1$ and hence are unassociated with the foreground cluster.

The other influence that the cluster may have is as a gravitational lens. However, A851 is not a particularly concentrated cluster (Seitz et al. 1996; Trager et al. 1997; Iye et al. 2000), and the wide-field coverage of our sample, compared with the cluster's critical radius (only two of the EROs in our sample lie within 1′ of the cluster center, roughly corresponding to 2–3 times the critical radius), suggests that lensing by the cluster will have a minimal effect on the surface density in our sample ($\lesssim 5\%$ integrated over the whole area of our survey) and is unlikely to grossly affect the morphologies of any of the EROs in our study.

2.1. *Radio Observations*

The radio image of A851 comprises a combination of A, B, C, and D configuration observations from the National Radio Astronomy Observatory's VLA[8] taken at 1.4 GHz between 1996 and 2000. For each observation, "4" mode was used for the correlator with 7×3.125 MHz spectral channels for each of two IFs and two polarizations. This mode was employed to allow a map to be made of the entire primary beam at the highest spatial resolution possible with the VLA ($\sim 1\farcs5$ FWHM) and with the best compromise between radial smearing of the image due to the finite bandwidth and sensitivity. However, as is noted below, some penalty does result from this choice. The total integration time of the combined data set is $\sim$100 hr on source.

The data set was imaged using the AIPS program IMAGR. The 74 facets were used, including 37 within the primary beam and 37 outside the primary beam, each of the latter centered on a bright confusing source. Each of the data sets from the four configurations was self-calibrated using intermediate images as input to the AIPS program CALIB. A more complete description of the reduction process is included in F. N. Owen et al. (2002, in preparation).

The analysis presented here focuses on the central facet from the full map, an $8\farcm53 \times 8\farcm53$ field in the center of the primary beam: $\alpha = 09^{\rm h}42^{\rm m}48\fs614$, $\delta = 46^\circ 59' 59\farcs72$ (J2000.0). The final map reaches a 1 σ noise level of 3.5 μJy beam^{-1} in the central part of this field, making this the deepest 1.4 GHz map ever made. However, in the extreme corners of the area being analyzed the actual peak flux density is reduced by about 20% as a result of the primary beam attenuation and radial bandwidth smearing caused by the finite bandwidth of each spectral channel. We therefore adopt a conservative 3 σ limit of 12.6 μJy in the corrected peak flux density over the entire area being studied. We can probe down to 3 σ significance limit and still retain a very low level of false detections as we are searching for radio emission at the known positions of a relatively small number of EROs, compared to the number of independent beams in our map (10^5). The synthesized beam of our final map is circular and has an FWHM of $1\farcs6$; this allows us to resolve radio sources with sizes $\gtrsim 1''$, and we discuss the sizes of radio emission from the EROs in our survey in the following sections.

[8] NRAO is operated by Association of Universities for Research in Astronomy (AURA), Inc., under a cooperative agreement with the National Science Foundation.

2.2. *Near-Infrared Observations*

Our primary near-infrared imaging data set comes from wide-field images in *JHK* taken with the KPNO 2.1 m telescope; these cover a $15\farcm4 \times 15\farcm7$ field of view to $K \sim 21$. These images have relatively coarse sampling, and so we have also obtained higher resolution *J* and *K* images covering a smaller ($7\farcm5 \times 7\farcm5$) field of view from the 4.2 m William Herschel Telescope[9] (WHT) and the 3.8 m UK Infrared Telescope[10] (UKIRT), respectively. The WHT and UKIRT observations cover the bulk of the region included in the analysis here and thus provide a useful confirmation of the identifications and photometry of EROs in this field. Standard reduction procedures were applied to all data sets and were calibrated using UKIRT Faint Standards (Hawarden et al. 2001).

2.2.1. *KPNO* 2.1 m *JHK-Band Mosaics*

The SQIID camera was used at the KPNO 2.1 m telescope on the nights of 2001 January 4–11 to image the field simultaneously in *JHK*. The pixel scale of the camera is $0\farcs68$, and the useful field of view is $\sim 5\farcm2 \times 5\farcm2$, with nine pointings mosaicked together to cover a region of $15\farcm4 \times 15\farcm7$. The total exposure time was 75 ks, spread equally over the nine pointings to give a per pixel exposure time of 8.3 ks.

The images were reduced in a standard manner using IRAF scripts. Flat fields were constructed from the dithered exposures at each pointing to produce a flat field centered in time on each exposure. Distortion corrections were measured from a comparison of bright objects in the near-infrared images with existing, deep *R*-band images, and these were applied to align the images in the three passbands to a common coordinate grid, at a level of 0.1 pixel rms or better.

These observations were obtained in a mix of photometric and nonphotometric conditions, with seeing of $1\farcs5$–$1\farcs8$ FWHM. To calibrate the photometry in the three bands, we exploit the precise *JHK* photometry of this field published by Stanford, Eisenhardt, & Dickinson (1995). By comparing the photometry for a large number of bright galaxies in the field we estimate a typical zero-point error of $\lesssim 0.03$ mag on our photometric scale. The total magnitude corresponding to the 5 σ detection limit for a point source is $K = 20.5$, while the 3 σ limits for $3''$ aperture photometry in the *J* and *H* bands are $J = 22.7$ and $H = 21.9$.

2.2.2. *UKIRT K-Band Mosaic*

On the nights of 1999 February 28, March 01–02, and March 15–16 we completed a *K*-band mosaic of 5×5 pointings using the UFTI imager on UKIRT (pixel scale $0\farcs0908$ pixel^{-1}). This mosaic covers the central $7\farcm5 \times 7\farcm5$ region of the cluster defined by the WFPC2 field (see § 2.3) and hence covers around 55% of the radio sample analyzed here. Each pointing has a total integration time of 2.4 ks and reaches a limit of $K \sim 20.0$ for point sources. The median seeing for

[9] The WHT is operated by the Isaac Newton Group on behalf of the Particle Physics and Astronomy Research Council (PPARC).

[10] UKIRT is operated by the Joint Astronomy Centre on behalf of PPARC.

these observations was 0.″5, and several of the mosaic tiles have 0.″35 seeing, while periods of sub-0.″25 seeing were experienced. These frames allow us to confirm the reality of EROs in the field and investigate the morphologies of the brighter examples.

2.2.3. *WHT J-Band Mosaic*

On 2000 December 11–12 we used the INGRID near-infrared imager (Packham et al. 2002) on the WHT to obtain a *J*-band image of the cluster core. This comprised a 2×2 mosaic of 2.4 ks exposures and covers the same region as the UKIRT mosaic, reaching $J = 22.7$ for a point source in 0.″70 seeing with 0.″242 sampling.

2.3. *Optical Observations*

The optical imaging to complement our deep near-infrared data sets was obtained from three facilities. We have two wide-field imaging data sets of this region. The first comes from Suprime-Cam on Subaru (courtesy of T. Kodama) and consists of very deep *RI* imaging of a $27' \times 27'$ field centered on the cluster core. We also have obtained similarly a wide-field KPNO 4 m image in the *z* band to bridge the spectral coverage of our optical and near-infrared data sets. Finally, an *HST*/WFPC2 mosaic of A851 has been observed in the F702W filter; this covers a $7.'5 \times 7.'5$ region around the cluster core, within the area studied here, and provides very detailed morphological information on the optically bright galaxies in this area (A. Dressler et al. 2002, in preparation; G. E. Morrison et al. 2002, in preparation). However, the relatively shallow surface brightness limit of the *HST* imaging, $\mu_R \sim 25.5$ mag arcsec^{-2}, means that these data are not useful for gauging the morphologies of all but the most compact of the 15 radio-detected and 27 radio-undetected EROs in this region (see also Dey et al. 1999; Smith et al. 2002b). For this reason we will not use the *HST* imaging in our analysis.

2.3.1. *Subaru RI Imaging*

Kodama et al. (2001) obtained deep, *RI* imaging of A851 using Suprime-Cam on the 8.3 m Subaru Telescope on the nights of 2001 January 21–22. Suprime-Cam has a $27' \times 27'$ field of view, imaged with eight 4k × 2k CCDs at a scale of 0.″20 pixel^{-1}. The conditions were photometric during the observations, with seeing of 1.″0 and 0.″7 in *R* and *I*, respectively. Total exposure times of 4.0 and 1.3 ks were obtained, resulting in 3 σ limiting magnitudes for point sources in 3″ diameter apertures of $R = 26.7$ and $I = 25.6$. The reduction and calibration of these data are described by Kodama et al. (2001).

2.3.2. *KPNO* 4 m *z Imaging*

The *z*-band imaging of A851 was obtained on the night of 2001 January 25/26 with the MOSAIC camera on the KPNO 4 m. These data cover a $36' \times 36'$ field with 0.″258 pixel^{-1} sampling. The processed image combined five individual exposures, shifted so the combination eliminated areas lost to gaps between individual CCD chips. After applying chip-by-chip sky flats, each exposure was projected onto an astrometric pixel grid and co-added with appropriate masking for gaps and bad pixels. The data were taken in photometric conditions, and the final 7.2 ks exposure has seeing of 1.″0 FWHM and a 3 σ limiting magnitude of $z = 24.1$ in our standard 3″ diameter aperture.

2.4. *Photometric Catalog*

To catalog near-infrared sources in the field of A851, we ran SExtractor (Bertin & Arnouts 1996) on the *K*-band image of the field, first convolving the image with a 2″ diameter top-hat kernel and then searching for sources with areas greater than the seeing disk above an isophote defined as $\mu_K = 22.8$ mag arcsec^{-2}.

As our measure of the total magnitudes of the sources in the image we adopt the scaled aperture magnitude, BEST_MAG, calculated by SExtractor. This magnitude is measured within an aperture that is 2.5 times the first-moment radius of the source, except in crowded environments when it is replaced with a corrected, isophotal magnitude (see Bertin & Arnouts 1996 for details). The 5 σ detection limit for point sources in our catalog corresponds to a total magnitude of $K = 20.5$, and we detect 1186 sources in the area spanned by our current VLA catalog (Fig. 1). This point-source detection limit should be representative of the completeness of our catalog for those compact galaxies with half-light radii less than our 2″ diameter detection filter (this includes the majority of the faint, near-infrared field population; Chen et al. 2002). However, our catalog selection will tend to miss galaxies with very extended disks even though their integrated magnitudes are above this point-source limit, and this may introduce a morphological bias into our sample selection (Martini 2001; Chen et al. 2002; Firth et al. 2002; Snigula et al. 2002). However, this is not a significant problem for our analysis as the primary goal is to determine the proportion of dusty and evolved EROs in published surveys, and the relatively good agreement between our measured ERO surface density and values published by other workers (see Fig. 2) suggests that our catalog suffers no stronger bias than is typical for such surveys.

To measure colors for galaxies in our *RIzJHK* imaging, we use fixed, 3″ diameter aperture photometry from seeing-matched frames. The optical and near-infrared images were aligned to the coordinate system defined by the KPNO *K*-band image with a typical tolerance of $\lesssim 0.''1$. The seeing on these frames was then matched to that of the poorest resolution images (the *J*/*H*/*K* band) by Gaussian convolution.

3. ANALYSIS AND RESULTS

Our analysis begins by constructing a SExtractor-based *K*-selected catalog of EROs in the field. We then align the radio and optical/near-infrared images to an rms accuracy of 0.″32 using the 90 brightest radio and *K*-band sources in the joint field. This allows us to search for matches for the EROs within the radio map. We note that our radio observations identify all three cataloged submillimeter galaxies in this field (Smail et al. 1999a, 2002a; Cowie, Barger, & Kneib 2002), and we discuss these further in Ledlow et al. (2002).

3.1. *The ERO Samples*

For this analysis we start from our *K*-selected galaxy catalog and identify galaxies brighter than $K = 20.5$ (5 σ) that have 3″ diameter aperture colors redder than the limit of $(R-K) = 5.3$, which we adopt as the definition of an ERO (see Pozzetti & Mannucci 2000). Based on this we identify 68 EROs in our field, equivalent to a surface density of (1.04 ± 0.12) arcmin^{-2} at $K = 20.5$ (the error bar simply reflects Poisson statistics, and we have applied an incompleteness correction of 20% to the number density of EROs

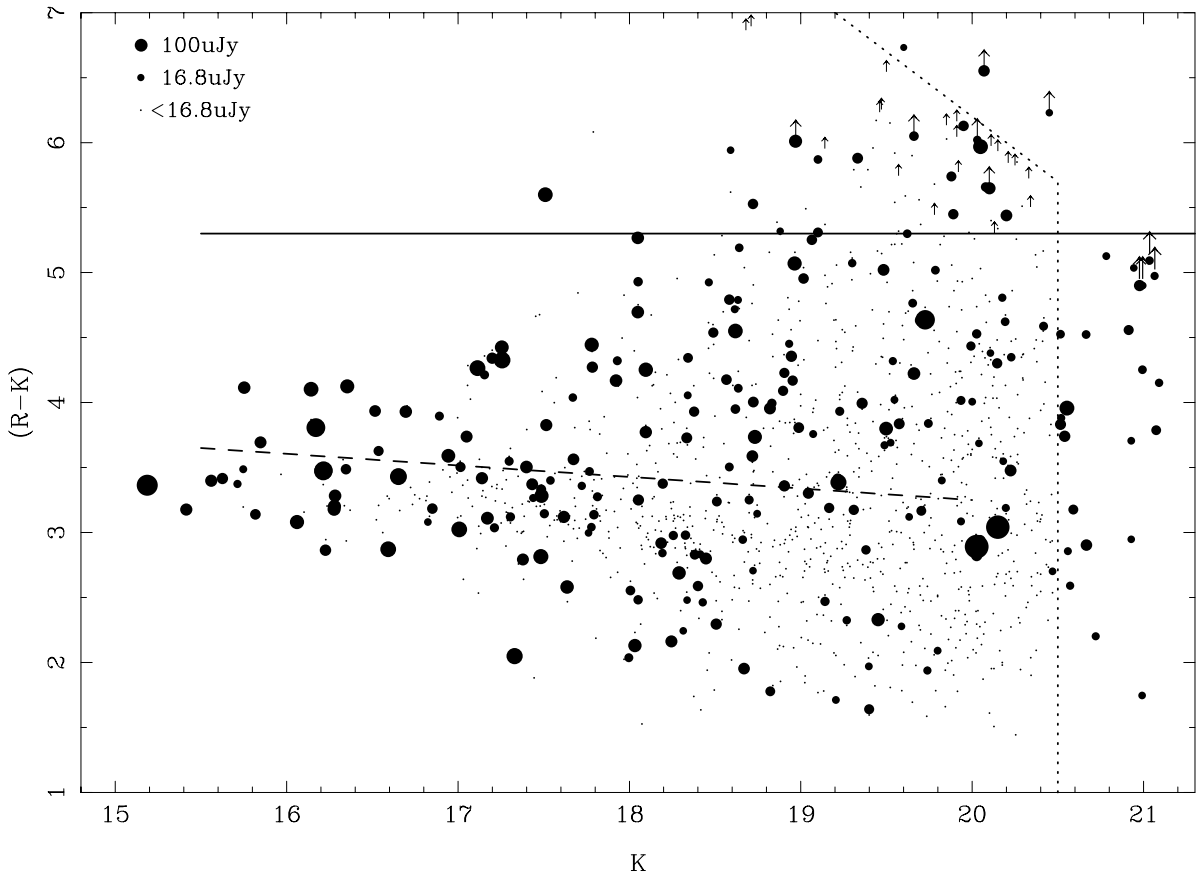

FIG. 1.—$(R-K)$–K color-magnitude diagram for 1186 sources brighter than $K = 20.5$ within an $8'.53 \times 8'.53$ field centered on A851; these are shown as small points and lower limits. Overlayed on this are the radio-detected sources brighter than the 4 σ limit of our radio map, 16.8 μJy. These radio sources go fainter than the nominal $K = 20.5$ catalog limit (*dotted line*). The solid line shows the $(R-K) = 5.3$ boundary used to define our ERO sample. For the ERO sample we identify all sources detected above a slightly deeper radio limit, 12.6 μJy or 3 σ, again indicating their radio fluxes by the size of the symbols used. The dashed line denotes the reddest color expected for unobscured galaxies at the cluster redshift; galaxies redder than this limit are likely to be beyond the cluster. The population of radio-emitting cluster members is clearly visible below this boundary (Morrison 1999; Morrison et al. 2002).

in the faintest bin, as well as a 6% correction to the area of the survey to account for the sky area covered by bright stars and galaxies).

The catalog of EROs in our field is given in Table 1. This lists the ERO identification (ID; a five-digit ID denotes a radio source), the J2000.0 position of the ERO (tied to the VLA reference frame with an rms precision of $0''.32$), the total K-band magnitude (measured using the SExtractor BEST_MAG), aperture $(R-K)$ color (or 3 σ limit), 1.4 GHz radio flux (or 3 σ limit), $3''$ diameter aperture magnitudes from our seeing-matched *RIzJHK* imaging, best-fitting SED (either dusty, "D"; evolved, "E"; or badly fitted, "B"; see § 3.5), and a visual morphology (from our high-resolution K- and R-band imaging if available; see § 3.4) on a simple system: "C" for compact/regular, "I" for disky, disturbed, or amorphous, and "F" for too faint to classify.

As is shown in Figure 2, the surface density of EROs we detect is in reasonable agreement with that observed in other ERO surveys (e.g., Thompson et al. 1999; Daddi et al. 2000; Smith et al. 2002b) given the strong field-to-field variation seen in the surface density of EROs (Daddi et al. 2001; McCarthy et al. 2001; Roche et al. 2002a; Chapman, McCarthy, & Persson 2000). This supports our claim that the foreground cluster makes no contribution to this population, either from members or by gravitational lensing. For ease of comparison with ERO samples selected in other filter combinations, in particular $(I-K)$, we note that while our field contains 68 EROs with $(R-K) \geq 5.3$, we have 99 objects with $(I-K) \geq 4$, suggesting that this is a less stringent definition of an unusually red source. We also note that 63 (93%) of our $(R-K) \geq 5.3$ EROs have $(I-K) \geq 4$ (including all of the radio-detected EROs from § 3.2).

We reidentify three previously cataloged EROs brighter than $K = 20.5$ in our field, including the submillimeter ERO SMM J09429+4658 from Smail et al. (1999a), which is also a faint radio source, and two other radio-undetected EROs: the edge-on disk galaxy 333 from the NICMOS study of Smail et al. (1999b) and Cl 0939+4713 A from Persson et al. (1993). A fourth cataloged ERO in this field, the passive $z = 1.58$ ERO Cl 0939+4713 B from Soifer et al. (1999), has $(R-K) = 5.1 \pm 0.1$ based on our photometry and hence does not make it into our ERO sample.

We can also use our UKIRT and WHT near-infrared imaging to test the reliability of our ERO sample. There are 30 EROs from the KPNO sample that fall within the UKIRT K-band and WHT J-band mosaics (11 of these are radio-detected). We identify 27 (90%) of these on the UKIRT mosaic. Two of the missing EROs are low surface brightness, extended systems that are below the detection limit of the UKIRT mosaic when using a large-diameter

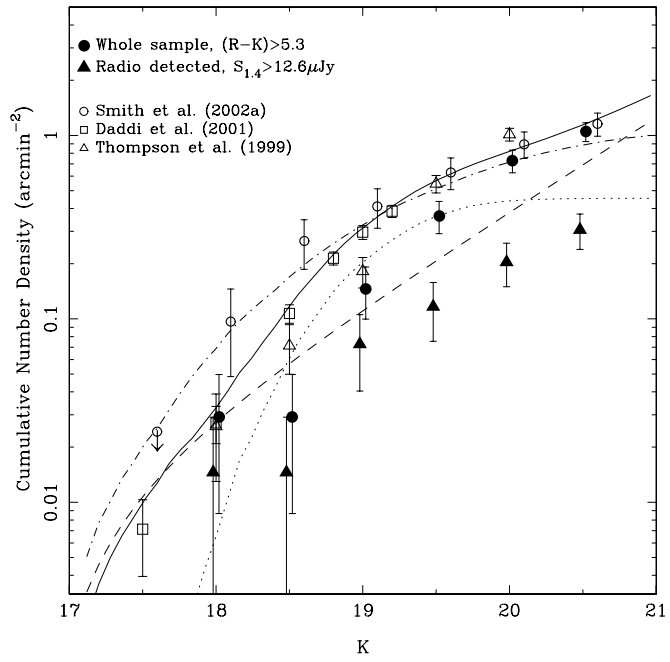

FIG. 2.—Cumulative number density of EROs in our sample compared to published counts from Daddi et al. (2000), Thompson et al. (1999), and Smith et al. (2002b). We show both the full ERO catalog, selected with $(R-K) > 5.3$, and also the radio-detected sample. The error bars represent simple Poisson uncertainties and are therefore likely to be underestimates of the true field-to-field variations (Daddi et al. 2001). We have included a 6% downward correction to the estimated area of our survey due to coverage by bright stars and galaxies in our field. The dashed line shows the fit to the radio-detected ERO population with a normalization increased to reproduce the 60% dusty ERO fraction estimated for our whole sample to $K = 20.5$. The dotted line is a Gaussian component with a mean magnitude of $K = 19.1$ and an FWHM of 1.2 mag that is normalized so as to reproduce the cumulative counts of EROs in our field. The solid line shows the behavior of a toy model constructed by combining the passive and dusty populations indicated by the dashed and dotted lines. The dot-dashed line shows a second toy model that combines a series of Gaussian luminosity functions for the ERO population with a mean of L_K^* and a dispersion of $\sigma_K = 1$ mag, which are co-added so as to produce a Gaussian redshift distribution with $\langle z \rangle \sim 1.1$ and $\sigma_z = 0.2$ (see Firth et al. 2002).

photometric aperture. This highlights the surface brightness, and hence morphological, biases that could affect the mix of morphological classes identified in ERO surveys (Chen et al. 2002). In this regard the good sensitivity, but relatively coarse, resolution of our KPNO *K*-band imaging acts in our favor by concentrating a large fraction of the light from the galaxy in a relatively small number of pixels (50 times fewer than in the UKIRT image).

The third "ERO" missing from the UKIRT mosaic is the source 2549 cataloged in the KPNO 2.1 m imaging (Table 1). This source is clearly detected in the simultaneously obtained *JHK* imaging from 2001 January 4–11 as a bright $K = 19.0$ unresolved source ($<1\farcs5$ FWHM) with unusual colors $(J-K) = 0.22 \pm 0.07$, $(H-K) = -1.09 \pm 0.07$, indicating that the SED peaks in the *H* band, yet it was apparently fainter than $K > 20.0$ during 1999 February (UKIRT) and $J > 22.7$ in 2000 December (WHT). In addition, we can state that the counterpart to this source was also fainter than our 3 σ limits of $R > 26.7$ and $I > 25.6$ on 2001 January 21 and $z > 24.1$ on 2001 January 25. The strongest constraint on the variability of the source comes from our *J*-band observations, which would indicate that the source brightened by 3.5 mag in a 1 month period, while our subsequent optical images suggest that it either was extremely red, $(I-J) \gtrsim 6.5$, or had faded by $\gtrsim 4$ mag within 3 weeks of the 2.1 m run. There are two possible explanations for the properties of this source: it is either moving (e.g., an asteroid or comet) or highly variable (e.g., a supernova, gamma-ray burst, or AGN). We can easily discount at least one of the variability options: if the source was a supernova, then it should still be visible in our optical imaging taken 3 weeks after the 2.1 m run. Equally, by subdividing our 2.1 m imaging into temporally independent sections and comparing the position of the object between these, we find no measurable movement of the source, $\lesssim 0\farcs5$, or strong variability over a 6 hr time span. If the object was moving at the maximum rate allowed by this limit, then it should still be visible within our *z*-band frame taken $\sim$3 weeks later. Its absence therefore rules it out as a solar system object. We conclude that 2549 is most likely a highly variable source, although unlike the highly variable AGN found by Gal-Yam et al. (2002), there is no optical or infrared host galaxy underlying 2549. We also note that 2549 lies 30″ from the variable X-ray source in this field cataloged by Schindler et al. (1998) and so is unlikely to be the same object.

Based on these comparisons we conclude that our photometrically selected ERO sample is reliable.

3.2. *The Radio-detected EROs*

We now search for radio counterparts to the EROs in our field. We adopt a maximum matching radius of 2″ (3 pixels on the near-infrared images) and search for radio emission above the 3 σ limit of 12.6 μJy centered on the *K*-band centroid of each ERO. Of the 68 photometrically selected EROs, 21 are detected in our deep VLA observations, giving a surface density of (0.31 ± 0.07) arcmin^{-2} for EROs with radio fluxes above 12.6 μJy and brighter than $K = 20.5$. The median *K*-band magnitude of these 21 EROs is $K = 19.66 \pm 0.22$ (Table 2), almost identical to the median brightness of the radio-undetected EROs: $K = 19.65 \pm 0.09$. The brightest ERO in the radio has a flux of only 200 μJy; we can therefore limit the proportion of radio-luminous AGNs in the general ERO population to $\lesssim 2\%$ (cf. Willott, Rawlings, & Blundell 2001).

The radio-detected EROs comprise $31\% \pm 7\%$ of the whole ERO population down to $K = 20.5$ (see also Yan 2001; Mohan et al. 2002), where the error bar is based on Poisson statistics and hence probably underestimates the field-to-field variance in this fraction. Taking the expected blank-field radio counts sources down to 12.6 μJy ($\sim$250; Richards 1999), the ERO counterparts with $K \leq 20.5$ represent $\sim$8% of the total radio population.

We plot the cumulative number density of the radio-detected EROs in Figure 2. We find, at most, marginal evidence for a difference in the count slope between the whole ERO population (and given our small sample also no strong evidence for a break in the count slope with magnitude) and the radio-detected and radio-undetected samples: parameterizing the counts as $\log_{10}(N_{\rm ERO}) \propto \alpha K$, we estimate $\alpha = 0.59 \pm 0.05$ for the whole catalog, with $\alpha = 0.51 \pm 0.08$ and $\alpha = 0.64 \pm 0.07$ for the radio-detected and radio-undetected samples, respectively.

The radio flux distribution of the radio-detected EROs is characterized by a strong rise at faint fluxes, the cumulative counts being well fitted by an $S_{1.4}^{-0.79 \pm 0.09}$ power law. Hence,

TABLE 1

ERO CATALOG

ID	R.A. (J2000.0)	Decl. (J2000.0)	K_{tot}	$(R-K)$	$S_{1.4}$ (μJy)	R_{ap}[a]	I_{ap}	z_{ap}	J_{ap}	H_{ap}	K_{ap}	SED[b]	Morphology[c]
01045	09 42 29.260	47 00 31.30	19.10	5.31	37.5	24.68 [03]	23.50 [06]	22.86 [11]	21.27 [13]	20.16 [08]	19.37 [07]	B	.../C
01049	09 42 29.750	47 03 22.50	18.72	5.53	44.4	25.00 [05]	24.01 [07]	23.12 [12]	21.57 [16]	20.57 [11]	19.47 [07]	D	.../I
01050	09 42 30.500	46 56 41.70	19.88	5.74	39.4	25.78 [08]	24.37 [09]	23.28 [13]	22.07 [26]	20.91 [17]	20.04 [11]	D	.../I
01053	09 42 30.610	47 00 21.70	17.51	5.60	195.6	23.65 [01]	22.28 [01]	21.18 [03]	20.32 [07]	19.17 [04]	18.05 [03]	D	.../I
01071	09 42 32.940	46 57 31.70	18.97	>6.01	112.2	>26.7	25.40 [30]	>24.1	>22.7	21.71 [27]	20.69 [17]	D	.../F
01081	09 42 34.140	47 00 14.40	20.20	5.44	70.2	25.81 [13]	24.83 [12]	>24.1	22.20 [24]	21.84 [31]	20.37 [13]	D	.../I
01105	09 42 37.980	47 01 20.90	19.33	5.88	51.9	25.78 [09]	24.06 [07]	23.45 [17]	21.84 [20]	20.36 [10]	19.91 [10]	B	.../I
01110	09 42 38.880	47 01 33.60	19.95	6.13	45.7	26.07 [14]	24.59 [11]	23.89 [33]	>22.7	21.26 [23]	19.94 [10]	D	.../I
01115	09 42 40.000	47 02 28.10	19.89	5.45	44.1	25.84 [11]	24.57 [12]	23.88 [26]	22.28 [23]	22.02 [31]	20.39 [12]	D	.../I
01118	09 42 40.340	47 00 16.30	18.88	5.32	16.0	24.71 [03]	23.55 [04]	22.51 [07]	21.33 [16]	20.53 [13]	19.39 [08]	D	I/I
01137	09 42 43.430	46 56 23.00	19.62	5.30	24.4	25.63 [10]	24.34 [09]	24.10 [31]	22.13 [21]	20.91 [12]	20.33 [12]	B	I/I
01150	09 42 44.840	46 56 37.50	19.66	>6.05	34.4	>26.7	>25.6	>24.1	>22.7	21.86 [30]	20.65 [16]	...	F/F
01157	09 42 46.250	46 59 30.20	20.07	>6.55	64.5	>26.7	>25.6	24.16 [33]	>22.7	>21.9	20.15 [10]	...	I/F
01176	09 42 49.970	46 57 40.60	20.08	5.66	32.9	26.08 [12]	24.52 [11]	>24.1	>22.7	20.91 [17]	20.41 [14]	D	I/I
01206	09 42 54.540	46 58 44.10	20.10	>5.65	81.1	>26.0	>25.6	>24.1	>22.7	>21.9	20.35 [20]	...	I[d]/F
01273	09 43 02.680	47 01 42.60	20.05	5.97	199.9	26.64 [18]	25.48 [23]	>24.1	>22.7	>21.9	20.66 [17]	D	F/F
01338	09 43 09.750	47 00 04.10	20.03	>6.02	23.2	>26.7	>25.6	>24.1	>22.7	>21.9	20.68 [21]	...	I/F
11018	09 43 13.067	46 55 50.07	18.59	5.94	17.0	25.34 [16]	23.76 [08]	22.96 [13]	22.62 [31]	21.14 [17]	19.40 [06]	B	I/I
11077	09 43 00.187	46 56 01.51	19.10	5.87	24.6	25.93 [14]	25.49 [24]	>24.1	>22.7	21.34 [21]	20.06 [12]	E	I/I
12861	09 42 58.729	47 03 39.62	19.60	6.73	14.1	26.54 [18]	24.56 [14]	23.98 [32]	22.06 [24]	20.70 [14]	19.81 [09]	B	.../I
13963	09 43 13.663	47 02 07.60	20.45	>6.23	16.3	>26.7	25.02 [17]	>24.1	>22.7	21.65 [30]	20.47 [15]	D	I/I
1091	09 42 27.721	46 56 07.02	19.47	>6.30	<12.6	>26.7	>25.6	>24.1	>22.7	21.75 [33]	20.40 [16]	...	.../F
1097	09 42 30.347	46 56 05.44	20.15	5.34	<12.6	25.59 [07]	24.46 [08]	23.43 [17]	22.58 [33]	>21.9	20.25 [13]	B	.../I
1136	09 42 40.436	46 56 13.55	19.69	5.56	<12.6	25.74 [17]	24.62 [19]	23.54 [23]	>22.7	21.36 [28]	20.18 [12]	D	F/C
1183	09 42 55.042	46 56 26.84	19.98	5.31	<12.6	25.54 [07]	25.82 [28]	>24.1	>22.6	21.12 [18]	20.23 [11]	E	I/I
1188	09 42 56.197	46 56 24.13	19.46	>6.28	<12.6	>26.7	>25.6	>24.1	>22.7	>21.9	20.42 [14]	...	F/F
1200	09 42 52.459	46 56 31.11	18.71	>6.94	<12.6	>26.1	24.27 [33]	>23.4	21.08 [12]	19.90 [08]	19.16 [06]	B	C/I
1206	09 43 04.291	46 56 32.52	19.91	>6.09	<12.6	>26.7	>25.6	>24.1	>22.7	>21.9	20.61 [17]	...	F/F
1321	09 43 01.416	46 56 59.37	19.52	6.15	<12.6	26.27 [19]	25.44 [29]	>24.1	>22.7	20.91 [16]	20.13 [10]	E	I/I
1349	09 42 36.967	46 57 06.70	19.55	5.54	<12.6	26.04 [15]	24.32 [11]	23.31 [14]	21.74 [17]	21.68 [30]	20.50 [15]	E	.../I
1473	09 42 54.991	46 57 37.60	19.35	5.66	<12.6	25.20 [10]	23.26 [05]	22.50 [08]	21.12 [12]	20.35 [11]	19.54 [07]	B	C/C
1523	09 42 55.919	46 57 46.88	19.57	5.32	<12.6	24.79 [09]	23.08 [07]	22.32 [08]	21.48 [17]	20.54 [14]	19.47 [08]	D	C[e]/C
1571	09 42 49.721	46 57 54.12	19.92	>5.82	<12.6	>26.7	>25.6	>24.1	>22.7	>21.9	20.88 [21]	...	F/F
1574	09 42 53.270	46 57 56.70	19.50	>6.59	<12.6	>26.7	24.29 [10]	23.54 [18]	22.05 [24]	21.29 [22]	20.11 [12]	D	I/I
1578	09 42 48.720	46 58 00.70	19.91	>6.21	<12.6	>26.7	>25.6	24.02 [34]	>22.7	>21.9	20.49 [14]	...	F/F
1762	09 42 35.264	46 58 38.27	19.56	5.30	<12.6	25.77 [07]	>25.6	>24.1	22.44 [31]	>21.9	20.47 [15]	E	.../F
1831	09 42 29.994	46 58 53.86	20.25	>5.87	<12.6	>26.7	>25.6	>24.1	>22.7	21.15 [18]	20.83 [21]	...	.../F
1931	09 42 59.183	46 59 17.34	18.68	>6.91	<12.6	>25.9	24.03 [16]	23.46 [27]	21.05 [12]	19.80 [08]	18.99 [05]	B	I[f]/I
1961	09 42 27.404	46 59 19.52	20.33	>5.77	<12.6	>26.7	>25.6	>24.1	>22.7	>21.9	20.93 [23]	...	.../F
1998	09 42 46.730	46 59 29.12	19.78	5.53	<12.6	25.41 [06]	23.83 [06]	22.95 [09]	>22.7	21.30 [19]	19.88 [08]	D	C/I
2047	09 42 45.795	46 59 36.12	20.26	5.85	<12.6	26.39 [13]	24.82 [15]	>24.1	22.17 [22]	>21.9	20.54 [16]	E	F/I
2128	09 43 12.079	46 59 58.69	18.86	5.39	<12.6	25.63 [16]	24.73 [19]	>24.1	22.83 [34]	21.16 [17]	20.25 [12]	D	I/F
2176	09 43 12.745	47 00 02.55	19.85	6.03	<12.6	26.24 [26]	25.10 [26]	24.06 [32]	22.75 [34]	21.77 [31]	20.21 [15]	D	C/I
2334	09 42 36.727	47 00 27.71	20.21	>5.89	<12.6	>26.7	>25.6	>24.1	>22.7	>21.9	20.81 [21]	...	.../F
2351	09 42 23.653	47 00 33.41	19.85	>6.18	<12.6	>26.7	>25.6	23.57 [34]	>22.7	>21.9	20.52 [17]	...	.../...
2405	09 42 34.421	47 00 44.61	20.29	5.51	<12.6	26.20 [15]	24.28 [12]	>24.1	22.36 [27]	21.41 [20]	20.68 [16]	E	.../I
2418[g].....	09 42 42.925	47 00 53.59	17.79	6.08	<12.6	24.20 [03]	20.95 [01]	19.82 [01]	18.95 [03]	18.37 [03]	18.12 [03]	B	.../C

TABLE 1—*Continued*

ID	R.A. (J2000.0)	Decl. (J2000.0)	K_{tot}	$(R-K)$	$S_{1.4}$ (μJy)	R_{ap}[a]	I_{ap}	z_{ap}	J_{ap}	H_{ap}	K_{ap}	SED[b]	Morphology[c]
2510	09 42 38.542	47 01 11.67	19.14	5.37	<12.6	24.99 [04]	23.53 [04]	23.06 [11]	21.51 [15]	20.34 [10]	19.61 [08]	B	.../I
2528	09 42 29.343	47 01 10.44	20.34	>5.55	<12.6	>26.7	>25.6	>24.1	>22.7	>21.9	21.15 [28]	...	.../F
2549[h].....	09 42 57.330	47 01 17.81	19.01	>7.61	<12.6	>26.7	>25.6	>24.1	19.31 [04]	18.00 [03]	19.09 [06]	B	.../F
2593	09 42 30.669	47 01 27.41	19.55	5.92	<12.6	25.85 [12]	24.48 [13]	23.20 [14]	>22.7	21.18 [18]	19.94 [10]	D	.../I
2637	09 42 36.916	47 01 37.91	19.42	5.96	<12.6	25.79 [10]	24.15 [10]	24.02 [34]	21.54 [16]	20.67 [13]	19.83 [09]	B	.../I
2762	09 43 07.026	47 03 08.20	20.11	>6.02	<12.6	>26.7	>25.6	>24.1	>22.7	>21.9	20.68 [20]	...	.../F
2769	09 43 01.067	47 02 59.08	19.57	>5.79	<12.6	>26.7	25.20 [23]	>24.1	>22.7	>21.9	20.91 [21]	...	.../F
2770	09 43 00.967	47 03 16.07	19.65	5.90	<12.6	26.48 [19]	25.29 [26]	23.66 [20]	>22.7	>21.9	20.58 [19]	D	.../I
2778	09 42 43.902	47 03 15.18	20.15	>5.98	<12.6	>26.7	>25.6	>24.1	>22.7	>21.9	20.72 [20]	...	.../F
2801	09 43 01.485	47 03 16.40	20.13	>5.35	<12.6	>26.7	>25.6	>24.1	>22.7	>21.9	21.35 [32]	...	.../F
2807	09 43 06.467	47 03 11.84	19.78	>5.49	<12.6	>26.7	>25.6	24.15 [32]	>22.7	>21.9	21.21 [28]	...	.../F
2862	09 42 30.473	47 03 17.54	19.03	5.49	<12.6	25.36 [06]	24.41 [09]	22.88 [10]	21.99 [23]	20.59 [11]	19.87 [09]	E	.../I
2972	09 42 26.348	47 03 45.41	19.39	5.79	<12.6	26.72 [28]	>25.6	>24.1	>22.7	>21.9	20.93 [23]	...	.../F
2976	09 42 28.057	47 04 00.26	19.14	>6.00	<12.6	>26.7	25.48 [26]	>24.1	>22.7	>21.9	20.70 [19]	...	.../F
2980	09 42 37.738	47 03 49.80	19.70	5.37	<12.6	26.03 [16]	>25.6	>24.1	22.69 [34]	>21.9	20.66 [20]	E	.../I
2984	09 42 30.238	47 03 44.30	19.61	5.59	<12.6	25.98 [12]	24.71 [13]	>24.1	21.84 [20]	21.44 [24]	20.39 [14]	E	.../I
3004	09 42 55.478	47 04 14.86	19.44	6.17	<12.6	26.62 [22]	25.33 [23]	23.84 [21]	22.24 [28]	21.36 [25]	20.44 [14]	E	.../I
3082	09 43 03.066	47 04 04.24	19.78	5.68	<12.6	26.30 [14]	25.92 [33]	24.10 [28]	22.09 [24]	>21.9	20.61 [15]	E	.../I
3732	09 42 37.383	47 03 32.32	18.59	5.62	<12.6	24.62 [04]	23.16 [04]	22.16 [05]	20.63 [08]	19.87 [07]	19.01 [05]	B	.../C
3930	09 42 53.314	47 02 05.63	20.11	5.40	<12.6	25.90 [09]	25.06 [19]	>24.1	>22.7	20.97 [15]	20.50 [12]	D	F/C
3942	09 42 27.216	47 02 09.18	19.31	5.79	<12.6	25.36 [06]	23.94 [07]	23.32 [16]	21.24 [11]	20.51 [10]	19.57 [07]	B	.../I

NOTE.—Units of right ascension are hours, minutes, and seconds, and units of declination are degrees, arcminutes, and arcseconds.

[a] Photometric errors in 0.01 mag are listed in square brackets.

[b] Best-fitting model SED: "D" for dusty, "E" for evolved, "B" for badly fitted.

[c] Morphological classification in K and R bands: "C" for compact/regular, "I" for disky, disturbed, or amorphous, "F" for too faint to classify.

[d] SMM J09429+4658 (Smail et al. 1999a).

[e] ERO Cl 0939+4713 A (Persson et al. 1993).

[f] ERO 333 (Smail et al. 1999b).

[g] M star.

[h] Transient source.

TABLE 2
MEDIAN COLORS OF ERO SUBSAMPLES

Sample	N	K	$(R-K)$	$(I-K)$	$(z-K)$	$(J-K)$	$(H-K)$	Dispersion	Note
Radio-detected									
All.....	21	19.66 ± 0.22	5.88 ± 0.13	4.53 ± 0.15	3.56 ± 0.08	2.05 ± 0.09	1.18 ± 0.08	0.37 ± 0.03	
Radio-undetected									
All.....	45	19.65 ± 0.09	5.82 ± 0.11	4.67 ± 0.14	3.40 ± 0.07	1.98 ± 0.06	1.05 ± 0.10	0.44 ± 0.03	Excluding 2418 and 2549
Dusty SED.....	9	19.67 ± 0.10	5.73 ± 0.19	4.51 ± 0.13	3.39 ± 0.18	2.53 ± 0.17	1.21 ± 0.11	0.36 ± 0.03	
Evolved SED	11	19.60 ± 0.11	5.59 ± 0.17	4.89 ± 0.20	3.49 ± 0.11	1.97 ± 0.14	1.18 ± 0.12	0.41 ± 0.07	
Badly fitted	8	19.22 ± 0.24	5.73 ± 0.32	4.27 ± 0.22	3.60 ± 0.37	1.81 ± 0.12	0.83 ± 0.04	0.49 ± 0.15	Excluding 2418 and 2549
Radio-detected and Radio-undetected									
Not fitted	20	19.92 ± 0.12	5.81 ± 0.13	4.94 ± 0.17	4.48 ± 0.45	2.19 ± 0.19	1.15 ± 0.15	...	

the number of EROs detected at 1.4 GHz rapidly increases at fainter flux limits: doubling as the flux limit is reduced from $\sim$40 μJy (typical of previous surveys; e.g., Richards et al. 1998) to the 12.6 μJy limit of the current work. At a flux level of around 50 μJy the ERO counts appear to increase more rapidly (perhaps indicating the appearance of a new population of very red and very faint radio sources) but then flatten out at faint fluxes. We believe that this flattening is probably a result of the depth of our available K-band imaging that is restricting the identification of the faintest and typically reddest sources (see Fig. 3). We see fairly constant K-band–to–radio flux ratios as a function of radio flux (see Fig. 3); this is in contrast to the strong decrease in this ratio with increasing radio flux above 1 mJy (Waddington et al. 2000), suggesting that a different physical process (star formation, rather than AGN activity) may be responsible for the faint emission from the sources in our catalog.

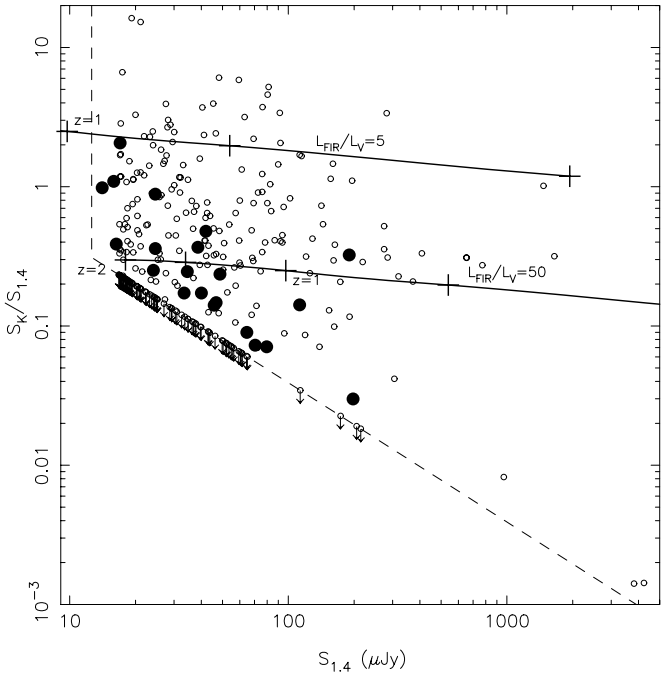

FIG. 3.—$S_K/S_{1.4\,\mathrm{GHz}}$–$S_{1.4\,\mathrm{GHz}}$ plane illustrating the variation in near-IR–to–radio flux with radio flux for all the radio-detected sources in our field. The dashed line shows the selection boundary for sources brighter than $K = 20.5$ and 12.6 μJy, and the filled symbols identify those radio sources that have ERO counterparts. We also illustrate the tracks for SEDs with far-infrared–to–optical flux ratios of $L_{\mathrm{FIR}}/L_V \sim 5$ and 50 (using the far-infrared/radio correlation for local galaxies; Condon 1992). We mark on these tracks the equivalent redshift limits (we mark $\delta z = 0.5$ increments on each track) assuming a model where the source is an $L_V^*(M_V = -21.8)$ galaxy with an SED similar to a present-day Sbc galaxy and radio luminosities of $L_{1.4} = 2.3 \times 10^{23}$ (*upper track*) and 2.3×10^{24} W Hz^{-1} (*lower track*) with a radio spectrum of the form $S \propto \nu^{-0.7}$. These radio powers are equivalent to SFRs of $\sim$20 and $\sim$200 $M_\odot$ yr^{-1} for stars above 5 $M_\odot$, respectively, or equivalently 10^2 and 10^3 $M_\odot$ yr^{-1} assuming a Salpeter IMF that extends down to 0.1 $M_\odot$ (see § 4.2).

The distribution of EROs in Figure 3 shows that these galaxies have typically lower near-infrared–to–radio flux ratios than average radio sources in the field (many of which are cluster members; G. E. Morrison et al. 2002, in preparation). The similarity of the K-corrections in these two wave bands over the redshift range we cover (see § 3.5) suggests that this is an intrinsic feature of these galaxies. Assuming that the local far-infrared–to–radio correlation holds for these galaxies, we conclude that the radio-detected EROs have far-infrared/optical ratios of $L_{\mathrm{FIR}}/L_V \sim 20$–200 (see § 4.2). Locally such high L_{FIR}/L_V ratios are usually only seen in the advanced stages of mergers of massive galaxies (e.g., Mirabel & Sanders 1989). In comparison, using the median K-band magnitude for the radio-undetected EROs we obtain a limit of $S_K/S_{1.4} \geq 0.6$, equivalent to $L_{\mathrm{FIR}}/L_V \lesssim 25$ (for an L_V^* star-forming galaxy at $z \gtrsim 1$ the equivalent FIR luminosity would translate into a limit on the star formation rate [SFR] of ≥ 0.1 $M_\odot$ stars of $\lesssim 100$ $M_\odot$ yr^{-1}).

Finally, we searched the archival 49.4 ks *XMM-Newton*/EPIC X-ray image of this field to identify any ERO that may be associated with a luminous X-ray source (Alexander et al. 2002; Stevens et al. 2002; Page et al. 2002). We find no such X-ray–bright EROs within our 72.7 arcmin^2 search region and place typical 3 σ limits on the unabsorbed X-ray emission from individual sources of less than 4×10^{-15} ergs s^{-1} cm^{-2} in the 2–10 KeV band.

3.3. *ERO Companions*

To search for differences in the local environment of the radio-detected and radio-undetected ERO populations, we look at the typical nearest neighbor distance in our $K < 20.5$ photometrically selected catalog (Georgakakis et al. 1999; Gallimore & Keel 1993). We note that the modest

spatial resolution of the KPNO *K*-band images means that this test is relatively insensitive to the presence of close companions, less than 1″–2″ separation. We find that the median nearest neighbor distance is $10\farcs9 \pm 1\farcs6$ for radio-detected EROs, compared to $15\farcs2 \pm 0\farcs8$ for those EROs that are not detected in our radio map. A Kolmogorov-Smirnov test shows only a 10% chance that the two nearest neighbor distributions are drawn from the same parent population. This suggests a higher frequency of neighbors for those EROs detected in our radio map, with separations roughly corresponding to ~100 kpc at $z \gtrsim 1$. However, these separations are probably too large for the companion to be responsible for dynamically triggering the activity in the radio source. To investigate the sub–10 kpc scales, where the signatures of ongoing mergers and strong dynamical interactions will be visible, we need to look at the detailed morphologies of the EROs (§ 3.4).

To further test the association of these neighboring galaxies with the EROs, we analyze their colors. We find that the radio-detected sample has a median nearest neighbor color of $(R-K) = 3.48 \pm 0.20$, while the closest $K < 20.5$ galaxies to the radio-undetected EROs have $(R-K) = 3.96 \pm 0.31$; in both cases the nearest neighbors have a median magnitude of $K \sim 19.2 \pm 0.2$. Both of these colors are marginally redder than the average for a magnitude-matched subsample from the field: $(R-K) = 3.26 \pm 0.05$, suggesting that the nearest neighbors to the EROs may lie at a higher mean redshift and are more evolved or more obscured than the typical field galaxy. Both samples also have comparable fractions of EROs as nearest neighbors: 14% of the radio-undetected sample have a nearest neighbor that is also an ERO [with $(R-K) \geq 5.3$] compared to 12% for the radio-detected EROs. Given that EROs make up only 6% of the whole *K*-band sample in this field, it is clear that the EROs as a population must be clustered (Daddi et al. 2001; McCarthy et al. 2001; Chapman et al. 2000).

3.4. *ERO Morphologies*

We can also exploit our high-resolution UKIRT *K*-band and Subaru *R*-band imaging to quantify the morphological mix within the two samples of EROs (Fig. 4). The UKIRT imaging provides rest-frame optical morphologies for 19 radio-undetected EROs (including the transient source 2549 [§ 3.1] and the star 2418 [§ 3.5]) and 11 radio-detected EROs. The properties of these subsamples are consistent with the full samples (Table 2) with median *K*-band magnitudes and $(J-K)$ colors of 19.61 ± 0.16, 2.09 ± 0.12 and 19.90 ± 0.24, 2.23 ± 0.12, respectively. In contrast, the Subaru *R*-band image covers the full ERO sample at slightly lower resolution but only gives us a rest-frame UV view of the morphologies of these galaxies, which is very sensitive to the presence of both dust and unobscured star formation.

We visually classify the EROs in both passbands using a simple scheme designed to crudely distinguish between regular, centrally concentrated galaxies, whose extreme colors may arise from an old stellar population, and more morphologically complex, disturbed or asymmetric galaxies, where their very red colors could indicate the presence of dust obscuration. Following Smith et al. (2002b), we define three broad classes: compact/relaxed systems ("C"); obvious disks, asymmetric or disturbed/amorphous morphologies ("I"); or too faint to reliably classify ("F"; see Table 1). Based on the near-infrared classifications we estimate that the morphologies of the radio-undetected ERO sample are five compact, five disks or disturbed/amorphous, and seven that are too faint to classify (29%:29%:42%), excluding 2549 and 2418. For the radio-detected sample the equivalent numbers are zero, nine, and two, respectively (0%:82%:18%). In both cases the uncertainties in the numbers in each class are probably one to two objects. We confirm that these two distributions are inconsistent with being drawn from the same parent population at the 10^{-4} level.

The morphological mix of the whole sample is 18%:50%:32%, identical to that measured for a $K \lesssim 21.5$ lensed sample by Smith et al. (2002b). We find a similar distribution when we use the rest-frame UV classifications from our *R*-band images, with the mix for the full sample being 11%:52%:37% and the radio-detected EROs having a slightly higher incidence of disturbed/amorphous morphologies and a lower incidence of compact images than the radio-undetected subsample. Thus, our sample appears to exhibit a lower fraction of compact, regular EROs compared to that presented by Moriondo, Cimatti, & Daddi (2000), where 80% of their EROs were classified as compact/elliptical-like from an analysis of a somewhat brighter (median $K = 19.3$) archival *HST* sample. This difference could reflect either a mismatch in the classification schemes, a tendency for the archival *HST* fields to target high-density regions, which may contain a higher fraction of bulge-dominated EROs, or a real change in the morphological mix of the ERO population with apparent magnitude (see § 4.2).

Turning to the internal differences within the subsamples of EROs in our survey, although the samples are small and the classifications are necessarily crude and somewhat uncertain, it appears that the radio-detected EROs show a higher incidence of disky and disturbed/amorphous morphologies compared to the radio-undetected sample, which in contrast has a higher fraction of compact sources (no examples of which are seen in the radio-detected sample). We illustrate a few examples of the various classes of ERO morphologies in Figure 4. We also briefly note the median $(J-K)$ colors of the different morphological classes (both radio-detected and radio-undetected): compact, $(J-K) = 2.02 \pm 0.36$; disky/amorphous, $(J-K) = 2.32 \pm 0.15$; faint, $(J-K) = 2.09 \pm 0.11$. Thus, there is a hint that the compact population is bluer than the extended (disky, disturbed, and amorphous) subsample, in agreement with the findings of Mannucci et al. (2002), but the large scatter in the colors of these subsamples suggests that they do not represent homogeneous populations.

Finally, we note that the radio emission from seven of the radio-detected EROs, 33% of the sample, is resolved in our map on scales of 0″.8–3″.4. The median intrinsic size of these sources is $1\farcs4 \pm 0\farcs4$, corresponding to 12 ± 3 kpc at $z \sim 1$ in our adopted cosmology. The remaining 14 radio-detected EROs are unresolved with a typical limit on the size of their radio emission of $\lesssim 0\farcs8$ (<7 kpc at $z \sim 1$). For the seven resolved EROs we can crudely compare their morphologies in the radio and optical passbands by determining the median offset in the position angles of the emission in these two bands. We find that the radio and *R*-band emissions have very similar scale sizes and that there is a median offset of only $11^\circ \pm 14^\circ$ between the position angles of the major axes in the two bands. This suggests that there is a close relationship between the extended radio and optical emission in these galaxies, and we return to this point in § 4.

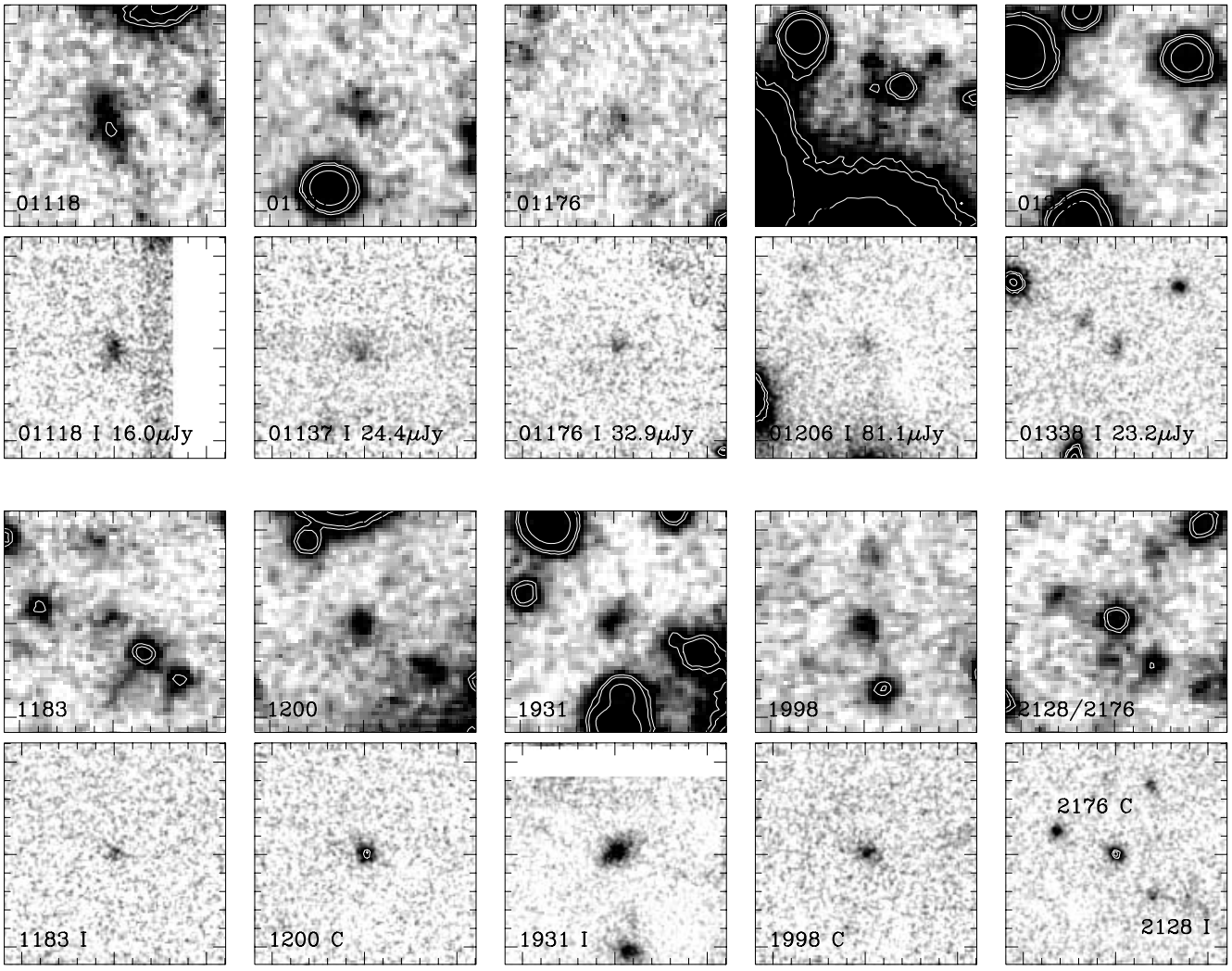

FIG. 4.—Example of the *R*- and *K*-band morphologies of a random selection of radio-detected (*top two rows*) and radio-undetected (*bottom two rows*) EROs that fall within the UKIRT mosaic. Each field is shown in two panels, with the Subaru *R*-band images above the UKIRT *K* band in both cases. We label the panels with the catalog number, *K*-band morphology, and radio flux (if detected). There is a clear tendency for radio-detected EROs to show more complex morphologies, while radio-undetected EROs are more regular and compact. We show two sources in the panel containing the compact ERO 2176 and an example of an amorphous, radio-undetected ERO: 2128. Note that 1931 is the edge-on disk galaxy identified in the NICMOS image from Smail et al. (1999b) and 01208 is the ERO counterpart to SMM J09429+4658 (Smail et al. 1999a). Each panel is $12'' \times 12''$ square and has north up and east to the left; the typical seeing is $0\farcs5$ in the *K* band and $1\farcs0$ in the *R* band.

3.5. *ERO Colors*

We begin our investigation of the colors of the EROs in this field by using the most basic diagnostic diagram proposed for this population: the $(R-K)$–$(J-K)$ plane. Pozzetti & Mannucci (2000) proposed that evolved and dusty EROs could be separated using this plane, with the passive, evolved EROs typically showing bluer $(J-K)$ colors (see also Smith et al. 2002b; Mannucci et al. 2002). We therefore plot the distribution of all the well-detected EROs (see below for the definition of "well-detected") on this plane in Figure 5. Focusing on the relative distribution of the radio-detected and radio-undetected EROs, we see that the radio-detected EROs tend to fall redward of, or close to, the division proposed by Pozzetti & Mannucci (2000). In contrast, the radio-undetected EROs show a much broader distribution, with roughly equal numbers of galaxies on either side of the division (see also Mannucci et al. 2002). Figure 5 also allows us to classify 2418 as a probable star (this is confirmed by the form of its SED in Fig. 6).

To investigate the photometric properties of the ERO populations in more detail, we now exploit our multiband photometry. We begin by simply constructing average colors for each sample. The median colors of the radio-detected and radio-undetected ERO samples are given in Table 2 (where the errors are the uncertainty on the median from bootstrap resampling). We find that the radio-undetected EROs are typically bluer than the radio-detected sample in colors longward of $\sim$1 μm, consistent with the color distribution of the two samples in Figure 5. We also find that the radio ERO population may be slightly more homogeneous than either the whole ERO catalog or the radio-undetected sample. For example, the radio-undetected sample exhibits a broader spread of colors with a typical dispersion of 0.44 ± 0.03 around the median color (Table 2), compared to 0.37 ± 0.03 for the radio-detected sample (this is also illustrated by the broader range of SEDs for the radio-undetected sample in Fig. 6). The varied mix of colors for the radio-undetected EROs is not surprising as we expect that this sample probably contains both passive

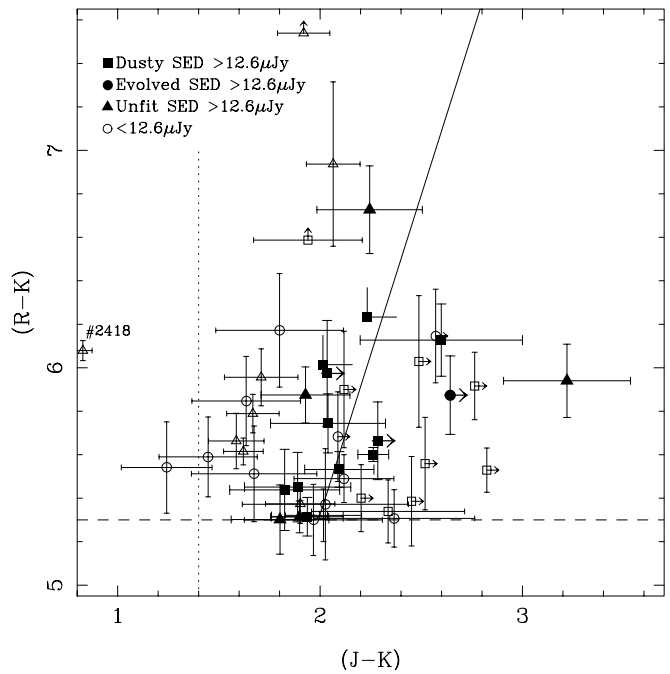

FIG. 5.—$(R-K)$–$(J-K)$ color-color diagram for the 47 high-S/N EROs brighter than $K = 20.5$ used in the SED fitting. We identify radio-detected and radio-undetected EROs using filled and open symbols, respectively, and in addition code the points depending on the better fitting SED: either dusty, evolved, or badly fitted. The solid line represents the boundary between dusty starburst and evolved, passive EROs proposed by Pozzetti & Mannucci (2000); the dusty galaxies should lie to the right of the line [redder $(J-K)$ colors], with the evolved systems on the left. Note that the high-S/N, radio-selected EROs lie either close to, or to the right of, this division, as do the majority of the high-S/N, radio-undetected EROs with dusty SEDs, confirming that the proposed boundary is reasonably effective. The dotted line divides low-mass stars from galaxies [which are redder in $(J-K)$]. The dashed line shows the $(R-K) = 5.3$ boundary used to define our ERO sample.

evolved galaxies and dusty active systems whose radio flux is below the sensitivity limit of our VLA map. The presence of passive, evolved galaxies in this sample is further supported by the more abrupt change in the colors of this sample at $\lesssim 1$ μm, corresponding to the 4000 Å break at $z \lesssim 1.5$. However, the relatively modest differences between the median colors of the radio-detected and radio-undetected samples also suggest that the radio-undetected ERO sample contains a reasonable fraction of galaxies with dusty SEDs (or that the relative redshift distributions of the two samples conspire so that the observed colors are more similar than they are in the rest frame).

3.5.1. *Photometric Classification of EROs*

To further investigate the photometric classifications of individual EROs, we have undertaken a simple test to determine whether the colors of a particular ERO are better described by a relatively featureless, dust-dominated SED or a spectrum with a strong break. The simplest way to apply this test is to employ the HYPERZ photometric redshift code (Bolzonella, Miralles, & Pelló 2000) to compare the ERO colors to two different families of SEDs: dusty, young starbursts (or AGNs) and almost dust-free evolved systems. For the dusty AGNs we assume that their optical and near-infrared colors are dominated by a coeval starburst (which produces the dust), although the AGNs may contribute significantly to the radio emission from the system. By relying on just two simple classes of SED we will clearly fail to describe any systems with more complex mixes of evolved stars and obscured and unobscured young stars (a situation that may be commonplace in many of these systems at high z, e.g., the edge-on bulge-strong disk galaxy ERO 1931; Fig. 4 and Table 1). However, by concentrating on those EROs that are well fitted by these simple models we can determine the relative proportion of EROs at the extremes of these classes.

For this test we employ a single star formation model described by an exponential declining SFR with an e-folding time (τ) of 1 Gyr, a Miller-Scalo IMF, and solar metallicity. This model can provide an adequate description of the colors of luminous elliptical galaxies at the present day (Bolzonella et al. 2000) and hence is a reasonable choice given the expectation that both the passive and star-forming ERO populations may represent the precursors of the elliptical galaxies seen in the local universe. As a test of the sensitivity of our classifications to the details of the star formation model we have also used an instantaneous burst and a $\tau = 2$ Gyr model in place of the $\tau = 1$ Gyr model and find that the proportion of EROs in the different classes varies by less than 10%.

In our model the initial formation redshift, the dust reddening, and the redshift of the ERO are all free parameters subject to the following constraints. For the starbursts/AGNs the reddening, based on a Calzetti et al. (2000) dust model, can vary in the range $A_V = 1$–6, consistent with the range of reddening estimated for their spectroscopically identified star-forming EROs by Cimatti et al. (2002). In contrast, for the passive models it is required to be $A_V < 0.5$; hence, by restricting the range of possible reddening we isolate the two families of solutions that are capable of fitting the very red colors of the EROs: either unobscured but old stellar populations or highly obscured, actively star-forming systems. In both cases the redshift of the ERO is allowed to vary between $z = 0$ and 3, a large enough range to comfortably encompass all of the EROs in Cimatti et al. (2002). The upper limit on the redshift removes the possibility of fitting infeasibly high redshifts as a result of the 4000 Å break being confused with the Lyman break, although we note that at least one ERO in our sample has a proposed redshift of $z > 3.4$ (01206; Smail et al. 2002a).

To obtain useful constraints from our analysis, we first require that the ERO is detected in at least three passbands at more than 3 σ; this reduces the samples to 17 radio-detected EROs and 30 radio-undetected EROs. We list at the bottom of Table 2 the median K-band magnitude and colors of those EROs that were removed from our analysis by this signal-to-noise ratio (S/N) cut. As expected, these are fainter on average, $K = 19.92 \pm 0.12$, than the typical ERO in our sample, which has $K = 19.63 \pm 0.09$. This magnitude difference is equivalent to that expected for a change in the median distance modulus of the population of $\delta z \sim 0.1$. As many of these EROs are undetected in a particular passband, we have improved the S/N of their colors by calculating these from the median fluxes in the various passbands, including cases in which the calculated flux is negative (Table 2). We find that these colors are consistent with those for the full samples, with the largest discrepancy being the $(z-K)$ color, which differs by ~ 2.2 σ. We conclude that the EROs removed by our S/N cut are at most slightly redder than the sample we retain, and the main reason for their lower S/N is that they are simply fainter on average.

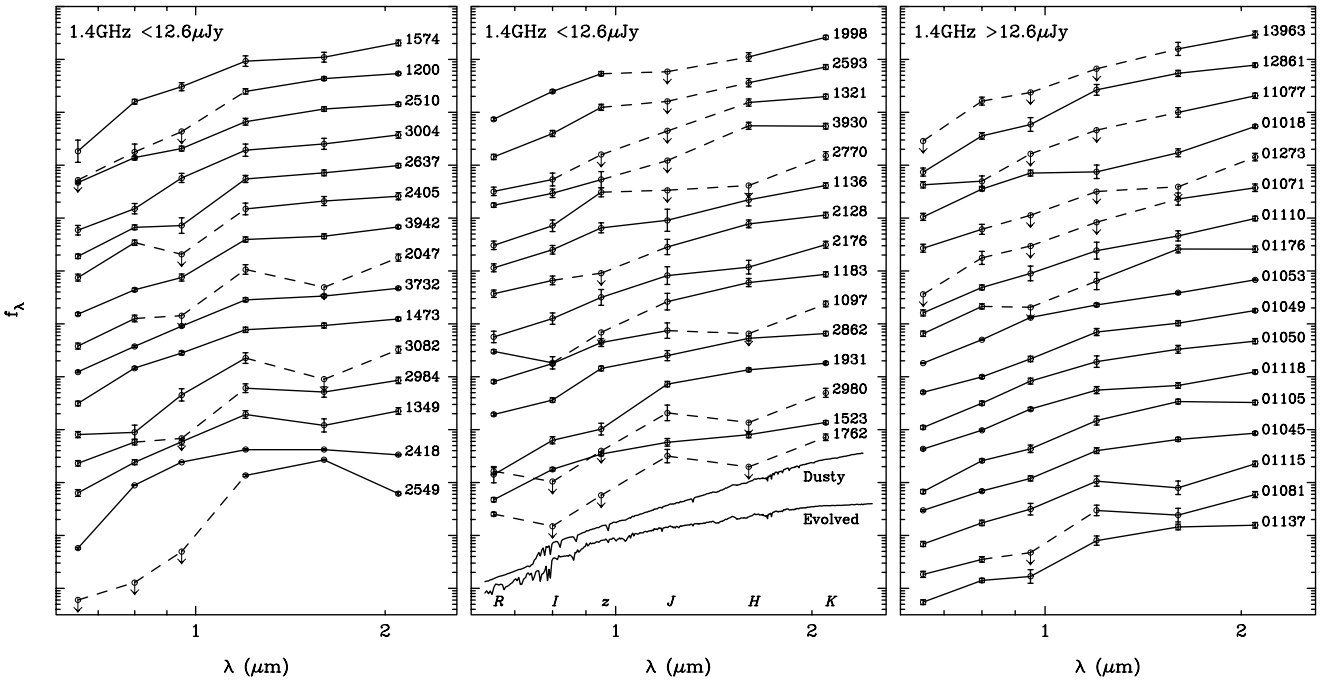

FIG. 6.—Broadband SEDs for the high-S/N, radio-detected and radio-undetected EROs from the sample used in our photometric analysis; each panel is ordered in terms of increasing $(J-K)$ color. The left-hand and middle panels show EROs that are undetected in our radio map, while the right-hand panel shows the SEDs for the 17 high-S/N, radio-detected EROs. These SEDs are plotted on an arbitrary flux scale, and we indicate uncertain regions of the SEDs by dashed lines. We also show an example of a dusty starburst SED and a passive, evolved galaxy, both at $z = 1$ at the bottom of the middle panel, as well as the central wavelengths of the six passbands used in our analysis. Note the peculiar SEDs of ERO 2418 and 2549; we identify 2418 as a late-type M dwarf (as suggested by its colors in Fig. 6), while the comparison of our independent *J*- and *K*-band observations of the field shows that 2549 is a transient source.

We fit the *RIzJHK* photometry (including limits) of the high-S/N radio-detected and radio-undetected samples to both families of model SEDs allowing for $\delta m = 0.05$ systematic errors on the calibrations of the different passbands. We then compare the relative χ^2 of the best-fit models in both cases and classify the EROs on this basis into either evolved ("E"), dusty ("D"), or badly fitted ("B"; see Table 2). We plot the SEDs of the sources used in the analysis in Figure 6. Encouragingly this test identifies 2418 and 2549 as pathological SEDs that are not well fitted by either galaxy model ($\chi^2 \gg 100$), and we remove these from our sample, reducing it to 28 sources (Table 2).

Restricting our comparison to those EROs that are reasonably well fitted by either SED, $\chi^2 < 2.7$ (90% confidence limit), we find that 12 of the 17 EROs in the high-S/N, radio-detected sample are well fitted, 11 of these by the dusty SED (65%). This supports the suggestion that the bulk of this population represent dusty, active galaxies and gives us good confidence that this model SED can be reliably used to identify dusty systems in the high-S/N, radio-undetected sample. We find only one radio-detected ERO that is better fitted by an evolved SED: 11077, a relatively faint radio source with an irregular ERO counterpart. Examining the SED of this source, we see that it is unique among the radio-detected EROs in having a blue $(R-I)$ color, which cannot be well fitted by a dusty SED (Fig. 6). Comparing the morphology of the ERO in the *R* and *K* bands, we find that the galaxy comprises two regions: a blue area to the east of the radio source and a very red area to the west. This complex morphology suggests that the simple model we use to fit may not be applicable to this galaxy.

The five high-S/N, radio-detected EROs that are not well fitted by the dusty SED (01045, 01105, 01137, 11018, and 12861) are ill fitted by either family of model SEDs ($\chi^2 > 5$–11). This could result from systematic errors in our photometry for these galaxies (although we have checked that their colors do not appear to be strongly effected by nearby galaxies) or from their SEDs not being well matched to the two simple alternatives used in our analysis: e.g., composite systems with evolved stellar populations and AGN contributions, galaxies with complex dust geometries, or very high *z* starbursts that are also not included in our model (e.g., Waddington et al. 1999). We will discuss the properties of these sources in the context of a fuller photometric analysis of the complete radio population in this field in F. N. Owen et al. (2002, in preparation).

Turning to the radio-undetected EROs, we find that 20 of the 28 sources (79%) are reasonably described by one or other of the two families of model SEDs. Of these, 11 (39%) are better fitted with a passive, evolved SED, compared to nine (32%) that are well fitted by a dusty SED. The median *K*-band magnitudes of the two classes are $K = 19.60 \pm 0.11$ for the evolved subsample and $K = 19.67 \pm 0.10$ for the dusty sources; if we include with the latter the 11 well-fitted dusty, radio-detected EROs ($K = 19.91 \pm 0.28$), we obtain a median magnitude of $K = 19.82 \pm 0.09$ for all of the EROs whose colors are well fitted by a dusty SED. Thus, there is a slight tendency for the EROs with dusty SEDs to be fainter than those with evolved SEDs. The eight radio-undetected EROs that are not well fitted with either family of model SEDs (ignoring 2418 and 2549) are surprisingly bright on average, $K = 19.22 \pm 0.24$. To test whether this results from an error in the relative calibration of our

photometry, we increase the estimate of the systematic errors in the relative calibration of the photometry from $\Delta m = 0.05$ to 0.2 and confirm that this does not significantly affect the average magnitude of the badly fitting SEDs, although it does reduce their number from eight to four, with the EROs making up the difference being equally classed as dusty and evolved systems. We also confirm that photometry of these badly fitted EROs is not unduly affected by crowding.

The median colors of the various subsamples of radio-undetected EROs are given in Table 2. The dispersion of the colors of the individual EROs in each subsample around their median is also listed there; these show that the dispersion within the subsamples of radio-undetected EROs classed as dusty or evolved is less than that seen for the whole sample. This confirms that, as expected, the photometric classifications isolate more homogeneous subsamples from the overall radio-undetected ERO population, with the exception of the badly fitted subsample, whose larger dispersion suggests that it still contains a mix of SED types.

3.5.2. *The Mix of Dusty and Evolved EROs*

The strong preference for fitting the colors of high-S/N radio-detected EROs with the dusty SED model (11/12 well-fitted examples) gives us confidence that this model can be reliably employed to identify similarly dusty, active systems in the radio-undetected ERO sample and hence estimate the prevalence of such galaxies in the full ERO population.

Taking the estimate that at least 20% (9/45) of the radio-undetected EROs have dusty SEDs and including the 11 high-S/N, radio-detected EROs with similar photometric classifications, we conclude that at least $\geq$44% (20/45) of those EROs with well-sampled SEDs have colors compatible with dusty starbursts, or $\geq$30% (20/66) of *all* EROs with $(R-K) > 5.3$ and $K < 20.5$ (median $K \sim 19.6$). This is consistent with the estimate of the proportion of dusty starbursts at $K < 19.2$ (median $K \sim 18.3$) of 33%–67% from Cimatti et al. (2002).

There are two different assumptions that can now be made to broaden this constraint: one addresses the failure rate for fitting dusty EROs with our model SED, the other with the number of dusty systems in the low-S/N ERO sample. Firstly, we could assume that the proportion of dusty SEDs in the high-S/N radio-detected sample is the same as that measured for those EROs with well-fitted SEDs, 92% (11/12), i.e., that the majority of the radio-detected EROs have dusty SEDs. Based on this we can then estimate the failure rate for fitting the colors of a dusty ERO with our model template as 5/16. Adopting the same failure rate for the dusty galaxies in the high-S/N radio-undetected sample, which have similar quality photometry, means that half of the badly fitted EROs are actually dusty galaxies (we would get the same estimate if we had simply proportioned the badly fitted ERO sample on the basis of the relative numbers of the successful fits). Hence, we would estimate that at least 46% (13/28) of the high-S/N radio-undetected EROs have dusty SEDs. Adding in the radio-detected EROs then leads to a lower limit of $\gtrsim$50% on the proportion of dusty starbursts in the full ERO sample. Secondly, we could assume, based on the overall similarity of their median colors, that the high-S/N EROs are representative of the full samples. If this assumption is adopted, then we would again conclude that a minimum of $\gtrsim$44% of the EROs in our full sample have colors that are well fitted by a dust-reddened starburst.

Hence, either of these assumptions would suggest that a minimum of about one-half of the $(R-K) > 5.3$ and $K < 20.5$ ERO population have colors consistent with those expected for dusty starbursts. As these two assumptions are independent, we can also combine them by applying the misclassification correction to the radio-detected and radio-undetected samples (giving 16/17 and 13/28) and then assuming that the relative proportions of EROs of the photometric types in the high-S/N samples apply independently to the full samples (yielding 20/21 and 21/45). In this way we estimate that perhaps $60\% \pm 15\%$ of the full ERO sample are distant, dusty starbursts/AGNs, with the remainder being passive systems (although these may also include a small number of very high redshift galaxies; e.g., Waddington et al. 1999). This estimate of the proportion of evolved and dusty EROs in the $K < 20.5$ population is of course also sensitive to the strong clustering of the passive ERO population.

Our photometric classification also provides some other information about the EROs, in particular the best-fit redshift and reddening. However, the limited precision of our photometry and the strong degeneracies between these parameters mean that they should be viewed with caution. For the high-S/N, radio-detected EROs, which are well fitted by the dusty SED, the median redshift is $z = 1.0 \pm 0.3$, with a quartile range of $z = 0.8$–1.5. This range is very similar to that seen in the spectroscopic survey of Cimatti et al. (2002) and gives us some confidence in the average properties we determine for this population. The median reddening for this sample is $A_V \sim 3.5 \pm 0.4$. For the radio-undetected EROs, those galaxies that are fitted with a dusty SED give a similar median redshift of $z = 1.0 \pm 0.2$ and a slightly lower reddening of $A_V \sim 2.0 \pm 0.5$. These estimated reddenings are consistent with that estimated for their composite spectrum of star-forming EROs by Cimatti et al. (2002), $A_V \sim 2.4 \pm 0.9$. For both subsamples the median K-band luminosity at the estimated redshifts corresponds to $M_V \sim -18.4 \pm 0.4$, or $M_V \sim -21.5$ when corrected for reddening. The unobscured luminosities of these galaxies would be comparable to L_V^* galaxies today; however, their young stellar populations would be expected to fade substantially, and so it is clear that these galaxies are likely to evolve into sub-L_V^* galaxies at the present day, unless the current starburst continues for $\gtrsim 10^8$ yr.

Next, we look at the relationship between our crude rest-frame visual morphologies and the preferred photometric classification for 28 EROs (eight radio-detected and 20 radio-undetected; Table 1). The morphological mix in both cases is similar to the proportions of the different SED types, if we interpret the compact EROs as passive, evolved systems (Mannucci et al. 2002). For the radio-undetected sample we find a broad equality between the classes: 29% : 29% : 42% for compact : disky/amorphous : faint, similar to 39% : 32% : 29% for the evolved, dusty, and badly fitted SEDs. Similarly, for the radio-detected sample, which is dominated by dusty SEDs, the morphological mix is 0% : 82% : 18%, compared to the distribution of SED fits, 6% : 65% : 29%. However, a one-to-one comparison for individual EROs shows that while the distributions appear to be telling the same story, the individual galaxies are much more mixed: half of those EROs with dusty SEDs have disky,

amorphous, or disturbed morphologies, but none of the EROs with passive SEDs have compact morphologies (this morphological class is almost evenly split between dusty SEDs and failed fits). We also note that there is no clear trend in the SEDs of those radio-detected EROs that are resolved in our VLA map.

To summarize, we place a firm lower limit of $\geq$30% on the proportion of dusty starbursts in the full $(R-K) > 5.3$ and $K < 20.5$ ERO population. Adopting two separate corrections for the number of dusty EROs that are missed either as a result of the failure of our photometric classification or because they were removed as a result of their poor photometry, we propose that $\gtrsim$45%–50% is a more realistic lower limit on the fraction of dusty EROs. Finally, by combining these corrections we suggest that the actual fraction of EROs with dusty starburst/AGN-like colors is probably close to $60\% \pm 15\%$.

4. DISCUSSION

4.1. *The Evolution of Dusty and Evolved EROs*

We have estimated the relative proportion of dusty, active and passive, evolved systems in the $K \leq 20.5$ ERO population. By comparing this to the mix of classes estimated for the $K \leq 19.2$ sample by Cimatti et al. (2002) we can identify any decline in either class of EROs that might be responsible for the apparent break in the ERO counts at $K \sim 19$–20 (McCarthy et al. 2001; Smith et al. 2002b). The similarity of the two estimates suggests that there is no evidence for a significant shift in the mix of these two subpopulations across $K \sim 18$–20, although it should be noted that the Cimatti et al. (2002) sample is selected using a slightly bluer color criterion, $(R-K) \geq 5$, which complicates this comparison. This apparent lack of a substantial shift in the nature of the ERO population may indicate that the break arises instead from the volume sampled, with $K \lesssim 20$ EROs populating a relatively narrow redshift range. This volume would be bounded at the low-redshift end by the requirement that the galaxy is observed at high enough redshift, i.e., sufficiently far into the rest-frame UV, to enable a dust-reddened starburst or evolved stellar population to appear extremely red, $(R-K) \geq 5.3$ (Daddi et al. 2001; Firth et al. 2002). Observationally this appears to require $z \gtrsim 0.8$–1 (§ 3.5; Cimatti et al. 2002). At the upper end the redshift limit may be imposed by either the luminosity function, passive blueing of the stellar population, or the increasing fraction of unobscured star formation in both subclasses of ERO (the continuity between high-z SCUBA galaxies and the radio-selected ERO population suggested below would argue against the latter suggestion). If the break in the counts is due to the surveys reaching beyond the volume containing the ERO population, then the $K \sim 19$ break (Fig. 2) should roughly correspond to M^* for a composite luminosity function with a Schechter form. This would imply that the characteristic luminosity of the ERO population is very similar to that seen in the local field, $M_V^* \sim -21.5$, and that the ERO luminosity function has a faint end slope, α, which is shallower than $\alpha \sim -0.7$ (the slope of the differential counts beyond the break). To illustrate this, we plot a toy model in Figure 2; this has a mix of Gaussian luminosity functions each with mean luminosity of $M_K = 24.3$ ($M^* + 0.7$ at $z = 0$; Cole et al. 2001) and a dispersion of $\sigma_K = 1$ (similar to the width of the luminosity function of elliptical galaxies locally). These are combined to produce a redshift distribution with a mean redshift of $\langle z \rangle \sim 1.1$ and a dispersion of $\sigma_z = 0.2$ (Cimatti et al. 2002; Firth et al. 2002), and the cumulative counts are calculated using a simple K-correction. Clearly this toy model (with some further tuning) can reasonably reproduce the ERO counts, indicating that a combination of a narrow luminosity function and a narrow redshift range is a sufficient, if not unique, explanation of the form of the counts of the whole ERO population across $K \sim 17$–21.

However, such a model has two obvious shortcomings: firstly, it requires that the evolutionary behavior of the dusty and passive ERO populations is similar, which seems highly unlikely; and secondly, the required evolution means that the dusty, active EROs selected in our radio map are distinct from the higher redshift and fainter counterparts to the SCUBA galaxies, rather than representing a simple continuity of the population to lower redshifts and brighter K-band fluxes. For these reasons we reject this model and construct a second toy model.

For the second model we assume that the number counts of dusty EROs are well described by the power-law slope estimated for the radio-detected population in § 3.1, but with a normalization increased to reproduce the $\sim$60% fraction of the $K < 20.5$ ERO population that we estimate have dusty SEDs. To this we add a Gaussian population representing the passive subpopulation and normalize the combined sample to reproduce the weighted cumulative surface density of EROs at $K < 20.5$ from Thompson et al. (1999) and Smith et al. (2002b). Representative parameters for the passive subpopulation require a mean magnitude of $K = 19.1$ ($M_K^* + 0.5$ at $z = 0$ assuming no evolution, or $M_K^* + 1.5$ assuming passive evolution from $z \sim 1.1$) and an FWHM of 1.2 mag. We illustrate the cumulative counts of both subpopulations and the combined population in Figure 2. We note that this model predicts that the relative proportions of dusty and evolved EROs for a $K < 19.2$ sample are 35%:65%, in agreement with the current limits from Cimatti et al. (2002). Clearly this model, even without elaborate tuning, can provide an adequate description of the current data, while at the same time providing continuity between the dusty EROs detected in our VLA map and the higher redshift and fainter counterparts to submillimeter sources (Smail et al. 2002a; Ivison et al. 2002), and we therefore prefer it. A clear distinction between the alternative models will come from extending the counts of EROs fainter, to $K \gtrsim 21$–23, and estimating the relative mix of evolved and dusty systems at these depths. However, the depth of the imaging required for such a survey, $R \sim 28$ and $K \sim 23$, will make it observationally demanding.

4.2. *Star Formation in the Dusty ERO Population*

The resolution of over one-third of the radio-detected EROs in our VLA map, along with the close correlation between the radio and optical morphologies of these EROs, suggests a common mechanism for the emission at these two wavelengths. The simplest explanation is that the emission in both bands is powered by massive star formation within an extended region, on a scale of $\sim$10 kpc. Thus, for at least one-third of the radio-detected EROs, star formation is likely to contribute the majority of the radio emission (this includes one of the brightest radio EROs, 01053). Furthermore, we note that using the median 1.4 GHz surface brightnesses of these resolved EROs and the star formation

calibration discussed below, they are expected to have high star formation surface densities: $\sim 4\ M_{\odot}\ \mathrm{yr}^{-1}\ \mathrm{kpc}^{-2}$, more than sufficient to drive powerful winds.

4.2.1. *The Fraction of AGN-dominated EROs*

To reliably quantify the star formation occurring in the complete radio-detected ERO sample, we must estimate the contamination from AGN-dominated systems. The AGN fraction in the whole microjansky radio population can be determined from the spectroscopic and morphological surveys of microjansky radio sources (e.g., Muxlow et al. 1999; Roche et al. 2002b). These suggest that at most 20% of radio sources at $\gtrsim 100\ \mu$Jy are likely to be AGNs. However, these estimates are typically based on samples of radio sources with brighter optical counterparts than the ERO sample analyzed here (and the AGNs tend to be the bluer sources in even these samples; Roche et al. 2002b; Waddington et al. 2000). Nevertheless, nonthermal emission is seen in a handful of well-studied EROs (Pierre et al. 2001; Willott et al. 2001; Smith et al. 2001; Cowie et al. 2001), indicating that AGNs are not completely absent from the ERO population, but the fraction of these in complete photometrically selected ERO samples is not well determined (Cimatti et al. 2002). The most useful constraint on this fraction for our purpose is that estimated from the number of ERO counterparts to faint X-ray sources (Alexander et al. 2001, 2002; Brusa et al. 2002; Mainieri et al. 2002). While we earlier confirmed that none of the EROs in our sample are associated with a luminous X-ray source, using archival *XMM-Newton* observations, much more stringent limits are now available on X-ray counterparts to EROs from recent *Chandra* and *XMM-Newton* observations of blank fields (which have lower backgrounds than our cluster field).

Alexander et al. (2002) identify six $(I-K) \geq 4$ and $K \leq 20.1$ X-ray sources in a 70.3 arcmin^2 region within the 1 Ms Chandra Deep Field–North exposure, giving a surface density of 0.085 ± 0.035 arcmin^{-2}. Based on the relative numbers of $(I-K) \geq 4$ and $(R-K) \geq 5.3$ sources and the number counts of $(R-K) \geq 5.3$ EROs, we would expect roughly $\sim 0.07 \pm 0.03$ arcmin^{-2} X-ray–detected EROs with $(R-K) \geq 5.3$ and $K < 20.5$. This estimate assumes that the X-ray–detected fraction is not a strong function of color or K magnitude, although we note that two of the six sources in the Alexander et al. (2002) sample have $(I-K) = 4.0$ and hence are borderline cases. Compared to our ERO surface density of (1.04 ± 0.12) arcmin^{-2} this indicates that around 10% of the ERO population are detected in very deep X-ray observations.

However, the *Chandra* exposure used by Alexander et al. (2002) is sufficiently sensitive that it will detect not only obscured AGN sources, $L_{\mathrm{X}} \gtrsim 10^{44}$ ergs s^{-1}, but also powerful star-forming galaxies at $z \sim 1$ (Ranalli, Comastri, & Setti 2002). If we instead restrict the X-ray sample to those EROs that are too X-ray–luminous to be ULIRG-like starbursts at $z \sim 1$, i.e., $L_{\mathrm{X}}(0.1\text{–}2.4\ \mathrm{keV}) \gg 4 \times 10^{42}$ ergs s^{-1} [twice the X-ray luminosity of the local X-ray–bright starburst NGC 3256, which has $\log_{10}(L_{\mathrm{FIR}}/L_{\odot}) \sim 11.8$; Moran, Lehnert, & Helfand 1999], then the number of probable AGN-dominated sources in the Alexander et al. (2002) sample would drop to three [two of which have borderline, $(I-K) = 4.0$, colors], or an estimated surface density of $\lesssim 0.03$ arcmin^{-2} using our ERO criteria. We conclude that at most 3% of the ERO population with $(R-K) \geq 5.3$ and $K < 20.5$ are likely to host energetically dominant AGNs. This is consistent with the estimates from ERO counterparts to hard X-ray sources detected by *XMM-Newton* in Franceschini et al. (2002), as well as the recent estimate that 1%–2% of the ERO population have hard X-ray counterparts by Brusa et al. (2002) and Mainieri et al. (2002).

While the occurrence of AGN-dominated sources in the ERO population is obviously low, the estimates derived above do not tell us how frequently radio-selected EROs are detected in the X-ray wave band. Fortunately, we can also crudely estimate this from the Alexander et al. (2002) survey. Three of the X-ray–detected sources with $(I-K) \geq 4$ in Alexander et al. (2002) are also detected in deep 1.4 GHz observations, and two of these have X-ray and radio emission consistent with an X-ray–bright starburst at $z \sim 1$, suggesting a surface density of ~ 0.02 arcmin^{-2} for X-ray–detected AGNs with microjansky ERO hosts, corresponding to $\sim 6\%$ of the whole radio-detected ERO population. This rate of AGN contamination is consistent with our identification of only one radio-detected ERO with an evolved SED (assuming that the radio emission from this galaxy arises from a weak AGN; see § 3.5), corresponding to 6% of the sample. We therefore adopt 6% as the AGN contamination in our sample and conservatively assume that the radio emission from any EROs hosting an AGN is dominated by the AGN.

4.2.2. *The Star Formation Density in EROs*

We can now use our ERO sample to estimate the star formation density in the most obscured starbursts at $z \sim 1$ (Cram et al. 1998; Serjeant, Gruppioni, & Oliver 2002; Haarsma et al. 2000). We calculate two estimates of the star formation density. First we take the minimum number of galaxies in our sample that are likely to be dusty, active systems based on the analysis of their optical/near-infrared SEDs: this subsample comprises 11 high-S/N, radio-detected EROs and nine radio nondetections and provides a conservative lower bound on the estimated star formation density.

Those radio-undetected EROs with dusty SEDs are likely to either be more distant or have typically lower SFRs (and hence radio fluxes) than the radio-detected examples. Based on the analysis in § 3.5.2 there is a hint that these galaxies have similar redshifts to the radio-detected EROs, but lower reddenings and hence perhaps lower SFRs (Hopkins et al. 2001). Using their estimated surface density and extrapolating the cumulative number counts of radio-detected EROs in our field from § 3.2, we would expect most of the dusty, radio-undetected EROs to have radio fluxes above $\sim 5\ \mu$Jy, and hence we assume that the typical dusty, radio-undetected ERO has a radio flux of $\sim 10\ \mu$Jy.

For the second estimate we adopt the incompleteness estimates for the photometric classification from § 3.5 and hence use 20 radio detections and 21 radio-undetected EROs. Simply summing the 1.4 GHz fluxes for these two subsamples, we obtain a total radio flux of $\geq 910\ \mu$Jy for the conservative case and 1370 μJy for the more realistic estimate (these include contributions from the radio-undetected starbursts of 90 and 210 μJy, respectively). Applying our estimated AGN contamination reduces both of these estimates by 6%; however, if this contamination preferentially affects the most luminous, unresolved radio EROs, then the radio fluxes could be reduced by as much as $\sim 15\%$ (roughly

half the difference between our "conservative" and "realistic" cases).

Hence, we estimate cumulative rest-frame 1.4 GHz luminosities from star formation in the two subsamples of $L_{1.4} > (8.0 \pm 1.3) \times 10^{24}$ W Hz and $L_{1.4} = (12.2 \pm 1.5) \times 10^{24}$ W Hz, respectively. These assume a K-correction based on a $\nu^{-0.7}$ spectrum typical of star-forming galaxies (Richards 1998), which gives a correction of $1.62^{+0.28}_{-0.12}$, where the error is dominated by the redshift range of the galaxies. We now use the local correlation between 1.4 GHz luminosity and far-infrared luminosity (Condon, Anderson, & Helou 1991) to convert this estimate into a cumulative far-infrared luminosity for the sample; we note that the validity of this correlation has recently been confirmed at the redshifts studied here by Garrett (2002). In this way we obtain cumulative far-infrared luminosities of $L_{\rm FIR} > (16.1 \pm 2.5) \times 10^{12}$ and $(24.3 \pm 3.7) \times 10^{12}\ L_\odot$, respectively. We estimate that these correspond to SFRs for $M \geq 5\ M_\odot$ of greater than 1450 ± 220 and $2180 \pm 330\ M_\odot\ {\rm yr}^{-1}$ using the conversion in Condon (1992). If we instead adopt the new calibration of Yun, Reddy, & Condon (2001), we would estimate SFRs roughly half of the quoted values (see also Carilli et al. 2002). However, for comparison with previous work we retain the Condon (1992) calibration. Assuming a Salpeter IMF from 0.1 to 100 $M_\odot$, these rates are $\sim$5.5 times higher.

To calculate the volume probed by our ERO sample, we use the photometric redshift estimates for the 20 radio-detected and radio-undetected EROs that are classed as dusty starbursts and find a quartile range of $z = 0.8$–1.5 (in reasonable agreement with the spectroscopically determined redshift range from Cimatti et al. 2002, $z = 0.8$–1.4; see Daddi et al. 2002), which gives a corresponding volume of $(1.1 \pm 0.2) \times 10^5\ {\rm Mpc}^3$ at a median redshift of $z = 1$. The quoted uncertainty corresponds to changing either of the bounds on the volume by $\delta z = \pm 0.2$ and encompasses the estimate we would derive if we had instead adopted the redshift range for EROs from Daddi et al. (2002).

Combining this volume with the SFRs, we estimate equivalent star formation densities of $\dot{\rho}_*(0.1$–$100\ M_\odot) > 0.073 \pm 0.018$ and $0.11 \pm 0.03\ M_\odot\ {\rm yr}^{-1}\ {\rm Mpc}^{-3}$ (if the AGN contamination is predominantly in the most luminous, unresolved radio sources, the latter estimate will fall to $\sim$0.09 $M_\odot\ {\rm yr}^{-1}\ {\rm Mpc}^{-3}$). We compare these measurements to other estimates of the star formation density in Figure 7.

Our measurement of the star formation density in the radio-detected ERO population at $z \sim 1$ is comparable to estimates of that in Hα-selected galaxies at these epochs (Yan et al. 1999) and greater than that seen in optically selected galaxies (Lilly et al. 1995; Connolly et al. 1997). There is little or no overlap between the ERO population used in our analysis and the classes of galaxies that are employed in these previous studies, and hence their contributions to the total star formation density are distinct. This implies that the activity in obscured galaxies makes a sizable contribution to the total star formation at $z \sim 1$, especially when allowance is made for the proportion of the obscured star-forming population that is missing from our ERO sample as a result of the escape of a small fraction of UV light. The significant contribution from obscured star formation at $z \sim 1$ confirms earlier claims by Flores et al. (1999) and Haarsma et al. (2000) and is particularly important as this era represents the peak in the star formation activity in the universe (note that when integrated over cosmic time, the distribution in Fig. 7 is highly peaked at $z \sim 1$–2). This result therefore extends the conclusions of the mid-infrared, submillimeter, and radio surveys that the use of obscuration-independent measures of the SFR is critical to reliably estimate the total star formation density, from $z \sim 2$–3 to the era when most of the stars seen in galaxies today were formed.

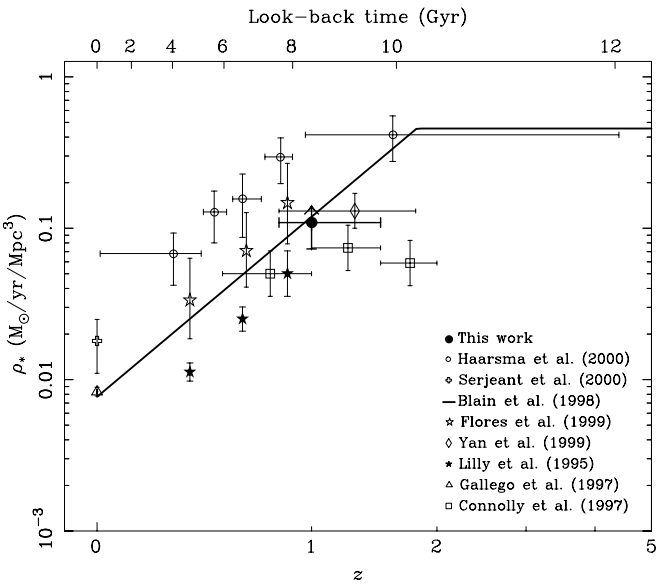

FIG. 7.—Evolution of the star formation density in the universe as measured using a range of long-wavelength tracers (which should be relatively insensitive to dust obscuration). We plot our measurement of the star formation density in the dusty ERO population; the lower limit of the error bar on this point corresponds to our conservative estimate of the star formation density in this population (see text). We compare this to other estimates from the radio (Haarsma et al. 2000; Serjeant et al. 2000), far-infrared/submillimeter (Blain et al. 1999b), mid-infrared (Flores et al. 1999), near-infrared (Connolly et al. 1997), Hα (Gallego et al. 1997; Yan et al. 1999), and UV/optical (Lilly et al. 1995).

4.3. *Dusty EROs in the Far-Infrared and Submillimeter*

We now estimate the volume density of the most strongly star-forming EROs. Based on the photometric redshifts for the 11 radio-detected EROs that are well fitted by a dusty SED, we estimate a median radio luminosity of $L_{1.4} = 10^{23.6 \pm 0.3}\ {\rm W\ Hz}^{-1}$ (compared to the Galaxy's radio luminosity of $L_{1.4} = 10^{21.4}\ {\rm W\ Hz}^{-1}$). Assuming that these galaxies follow the local radio–far-infrared correlation, this translates into a median far-infrared luminosity of $L_{\rm FIR}/L_\odot = 10^{11.9 \pm 0.3}$ for the subsample. The brightest five EROs in this subsample have inferred far-infrared luminosities above $L_{\rm FIR} \geq 10^{12}\ L_\odot$, which classes them as ultraluminous infrared galaxies (ULIRGs). Based on these five galaxies we estimate a surface density of radio-detected ULIRG EROs of $0.07 \pm 0.03\ {\rm arcmin}^{-2}$. This estimate could be increased by a factor of 1.4 to account for radio-detected EROs that are not well fitted by our model SEDs, although equally any increases should be offset against any AGN contribution to the radio luminosities of these galaxies.

Using the volume containing the dusty ERO sample given in § 4.2, we estimate an equivalent space density of ULIRG EROs as $\sim(0.5 \pm 0.2) \times 10^{-4}\ {\rm Mpc}^{-3}$ [and $\sim(2.7 \pm 0.4) \times 10^{-4}\ {\rm Mpc}^{-3}$ for all dusty EROs brighter than $K < 20.5$]. This is significantly higher than the space density of compa-

rable luminosity events locally, 0.03×10^{-4} Mpc^{-3} (Sanders & Mirabel 1996), even before allowance is made for the fact that some high-z ULIRGs will be missing from our ERO selection as a result of their blue colors (Trentham, Kormendy, & Sanders 1999; Goldader et al. 2002). Based on the far-UV colors of local ULIRGs it appears that more than half of this population would be too blue at $z \sim 1$–2 to be included in our ERO sample. Hence, if local ULIRGs are good analogs for the events that produce the high-z ULIRG population, then our volume density of $z \sim 1$ ULIRGs would require an upward revision by a factor of $\gtrsim 2$. We conclude that there has been *at least* an order-of-magnitude decrease in the number density of these luminous infrared events between $z \sim 1$–2 (8–10 Gyr ago) and the present day. This trend is consistent with the evolutionary models of Blain et al. (1999b), which also fit the number counts of SCUBA galaxies at higher redshifts (Fig. 7).

We can also estimate the submillimeter fluxes from the radio-detected EROs and hence investigate their relationship to the 850 μm selected samples detected by SCUBA. Based on the individual radio fluxes and estimated redshifts for the EROs we would predict a median 850 μm flux of 2 mJy and a range of 0.3–5 mJy (Carilli & Yun 2000). This places the bulk of these galaxies below the flux limit of typical SCUBA observations of faint radio sources (e.g., Chapman et al. 2001) and at least half of them below the confusion limit of the deepest (unlensed) SCUBA surveys. Clearly the radio/ERO selection allows us to probe the star-forming population to lower SFRs (and also lower redshifts) than typically achieved in submillimeter surveys as demonstrated by our detection of all three cataloged submillimeter sources in our field (see Ledlow et al. 2002).

Nevertheless, the most luminous radio-detected EROs should overlap with samples of ERO counterparts to SCUBA galaxies. We can test this by comparing the surface densities of these two populations. Our estimate of the surface density of $\gtrsim 2$ mJy radio-detected EROs is 0.07 ± 0.03 arcmin^{-2} at $K \leq 20.5$. This can be compared to the claim that $13\% \pm 9\%$ of the counterparts to SCUBA galaxies brighter than 2 mJy have $K \leq 20.5$ and $(R-K) \geq 5.3$, equivalent to a surface density of $\sim 0.11 \pm 0.09$ arcmin^{-2} (Smail et al. 1999a, 2002a; see also Mohan et al. 2002) and the estimate surface density of EROs brighter than 8 mJy of 0.03 arcmin^{-2} from Ivison et al. (2002). Allowing for the large uncertainties in these estimates and the possible upward revision of the density of radio-selected ULIRGs to account for badly fitted SEDs (including the known SCUBA ERO 01206), we conclude that they are in reasonable agreement. This suggests that by combining sensitive radio and submillimeter surveys it will be possible to track the evolution of the star formation density in highly obscured galaxies from $z = 0$ to $z \gtrsim 3$–5 (F. N. Owen et al. 2002, in preparation; Chapman et al. 2002a).

Finally, we estimate the contribution from the dusty ERO population to the far-infrared background at a wavelength corresponding to the peak of their dust emission: $\lambda = (1+z)\lambda_{\rm peak} \sim 120$ μm. Scaling from the 1.4 GHz emission, we estimate that the dusty ERO population produces $\nu I_\nu \sim 1 \times 10^{-9}$ W m^{-2} sr^{-1} at ~ 100 μm, compared to estimates of the background at this wavelength of $\nu I_\nu = (2 \pm 1) \times 10^{-8}$ W m^{-2} sr^{-1} (Hauser et al. 1998; Lagache & Puget 2000). Thus, the dusty EROs could contribute $\sim 5\%$–10% of the far-infrared background at its peak at ~ 100 μm. This compares to the SCUBA population, which produces $\sim 100\%$ of the background at 850 μm (Blain et al. 1999a; Smail et al. 2002a; Cowie et al. 2002) and probably the bulk of the far-infrared background at $\lambda \gtrsim 200$ μm (where the dust emission peaks for a population with a characteristic temperature of 40 K at $z \sim 2$–3). Both the dusty ERO and the SCUBA populations contribute $\ll 1\%$ of the extragalactic background at 1 μm, underlining the very different nature of the populations selected in the optical and the submillimeter/radio wave bands.

4.4. *The Passive ERO Population*

Our suggestion that at least half of the faint ERO population are dust-enshrouded starbursts obviously reduces the estimated volume density of passive, evolved EROs. We estimate that passive EROs at $z \gtrsim 1$ have a volume density of $\sim (3.6 \pm 0.6) \times 10^{-4}$ Mpc^{-3} for galaxies with a typical luminosity of $M_V \sim -20.6 \pm 0.4$. Passive evolution of the stellar populations would produce ~ 0.9 mag of brightening in the observed K band to this redshift, meaning that these galaxies would have $M_V \sim -19.7 \pm 0.4$ at the present day if they evolve passively. This assumes that the passive EROs inhabit the same volume estimated for the dusty ERO population, although as we discussed in § 4.1, these systems may lie in a smaller volume, and hence this volume density should be taken as a lower limit. In this regard we note that the $K < 19.2$ passive sample from Cimatti et al. (2002) has $z \sim 1.04 \pm 0.15$, where the error represents the 1 σ dispersion, and a quartile range of $z = 0.8$–1.2, somewhat narrower than the redshift range we use and suggesting a volume for the sample closer to 0.6×10^5 Mpc^3. Adopting this volume would roughly double our estimate of the volume density of passive EROs.

The most frequently proposed local analogs to passive EROs are elliptical galaxies, although it is clear that apparently passive EROs embrace a wider cross section of the $z \sim 1$ population than just diskless bulges (Smith et al. 2002a). It is consequently difficult to compare the volume density of this population with that of their possible descendants at the present day. However, we note that the combination of our reduction in the proportion of passive galaxies in the ERO population, coupled with the increase in the diversity of their morphological counterparts identified by Smith et al. (2002a), means that previously well-fitting pure luminosity evolution models with a high redshift of formation, $z > 2$, will now overpredict the ERO counts at $K \sim 20$ (Daddi et al. 2000; Firth et al. 2002; Smith et al. 2002b). This suggests that there may be some scope for the recent formation (or transformation) of some fraction of the local elliptical galaxy population (e.g., Aguerri & Trujillo 2002). Nevertheless, the reduction in the proportion of passive systems in the ERO population is still not sufficient to reconcile the observed surface density of evolved EROs with that predicted by semianalytic galaxy formation models (Smith et al. 2002b; Cole et al. 2000).

The proposed reduction in the passive ERO fraction also has ramifications for several previous results based on the properties of the whole ERO population. The most obvious is the interpretation of the strong clustering signal seen in ERO samples (Daddi et al. 2001, 2002; McCarthy et al. 2001). The strong angular clustering of the ERO population, especially for the brightest examples, appears to vindicate the predictions of hierarchical galaxy formation models assuming that these galaxies represent the passive, evolved

progenitors of present-day ellipticals (Firth et al. 2002). In the same manner, the apparent agreement between the angular clustering of Lyman break objects at $z \sim 3$ and theoretical models of halo clustering has provided support for the suggestion that these objects are the progenitors of massive ellipticals (Giavalisco & Dickinson 2001).

However, the presence of a large proportion of (perhaps weakly clustered) dusty EROs in the bright ERO population would tend to dilute the angular clustering signal arising from the strongly clustered passive EROs, unless there is a strong cross-correlation between the two populations (see Daddi et al. 2002 and § 3.3). Indeed, a further element comes into play when attempting to interpret the projected clustering of ERO samples: the redshift depth of the volume containing the galaxies. If the passive ERO population lies in a relatively narrow redshift range (see the toy models in § 4.1; Firth et al. 2002), then the dilution effect from the depth of the sample will be less than anticipated, requiring an intrinsically less strongly clustered population to produce a given angular clustering signal (Daddi et al. 2001). Thus, the effects of a narrower redshift depth for the evolved ERO subsample and the increased proportion of weakly clustered, but typically faint, dusty EROs may cancel each other out, leaving the estimated correlation length for the bright, evolved EROs close to that required for the progenitors of the L^* elliptical galaxies seen in the local universe, as estimated by Daddi et al. (2001) and McCarthy et al. (2001). We conclude that the complex interplay between the sample volume and the mix of evolved and obscured galaxies in the ERO population as a function of apparent magnitude means that the interpretation of the angular clustering of this class of galaxies is far from trivial.

5. CONCLUSIONS

The main conclusions of this work are as follows:

1. We catalog 68 EROs within a 72.8 arcmin^2 field that has the deepest 1.4 GHz observations of any region on the sky. We find that 31% of these EROs are detected in the radio map down to a flux limit of 12.6 μJy. Of these radio-detected EROs, 33% are resolved in our VLA map with a typical FWHM of $1\farcs4 \pm 0\farcs4$, equivalent to 12 ± 3 kpc at $z \sim 1$. Moreover, the radio emission in these EROs mirrors their R-band morphologies, suggesting that star formation is responsible for the bulk of the radio flux.

2. Using our deep $RIzJHK$ imaging, we photometrically classify the radio-detected and radio-undetected EROs into dusty or evolved systems based on simple SED models. We first analyze the colors of those radio-detected with high-quality photometry and conclude that the majority of these are adequately described by a highly dust-reddened starburst spectrum. This provides support for applying this analysis to the radio-undetected EROs to search for similar obscured, active galaxies.

3. Using our simple photometric models, we estimate that more than 32% of the radio-undetected EROs with high-quality photometry, or a minimum of 20% of all radio-undetected EROs, have the colors of dusty starbursts, similar to the radio-detected EROs. We estimate the rate of misclassification of EROs in our analysis assuming that most of the radio-detected EROs are actually dusty starbursts, and based on this we propose that $\sim$45% of the EROs with radio fluxes less than 12.6 μJy have dusty SEDs. From the continuity of the number counts of radio-detected EROs we would expect that most of these sources would have 1.4 GHz fluxes around 5 μJy. We also find that one of the 68 EROs has an SED consistent with a galactic star, while another apparent ERO appears to be a transient source.

4. Combining the samples of radio-detected and radio-undetected EROs that are photometrically classified as dusty, we place a firm lower limit of $\geq$30% on the proportion of dusty starbursts in the whole ERO population. To obtain a more realistic estimate, we adopt a correction for misclassification and assume that the resulting proportions of dusty and evolved EROs are representative of the full sample (not just those with the best photometry). We estimate that at least 45%–50%, and possibly up to $\sim 60\% \pm 15\%$, of the *whole* ERO population with $(R-K) \geq 5.3$ and $K \leq 20.5$ are probably dusty, active galaxies. Our fitting procedure also suggests a median redshift of $z \sim 1.0 \pm 0.3$ with a quartile range of $z = 0.8$–1.5. This is in reasonable agreement with the spectroscopic survey of somewhat brighter and bluer EROs by Cimatti et al. (2002). Assuming that AGNs do not dominate the radio emission from these galaxies, we estimate a volume density of EROs with far-infrared luminosities of $\gtrsim 10^{12}\ L_\odot$ (i.e., ULIRGs) of 0.5×10^{-4} Mpc^{-3}; this is over an order of magnitude higher than for equivalent luminosity events at $z = 0$ and confirms the strong evolution of the most dusty, active galaxies out to $z \gtrsim 1$ (Blain et al. 1999b).

5. We use the local far-infrared–radio correlation to estimate SFRs from the radio fluxes of the dusty EROs, assuming that their radio emission is purely powered by massive star formation. Combining these estimates with the probable volume spanned by our dusty ERO subsample, we can calculate the star formation density in this obscured population. Adopting conservative assumptions, we find that the star formation density in star-forming EROs at $z \sim 1$ probably exceeds $\dot{\rho}_*(0.1\text{–}100\ M_\odot) > 0.073 \pm 0.018\ M_\odot\ \mathrm{yr}^{-1}\ \mathrm{Mpc}^{-3}$ and may be as high as $\dot{\rho}_* = 0.11 \pm 0.03\ M_\odot\ \mathrm{yr}^{-1}\ \mathrm{Mpc}^{-3}$. This measurement is comparable to estimates of the star formation density in Hα-selected galaxies at these epochs and greater than that seen in optically selected galaxies, showing that the activity in obscured systems may make a significant contribution to the total star formation at $z \sim 1$. We also estimate that the dusty ERO population may produce up to 5%–10% of the far-infrared background at its peak at $\sim$100 μm, underlining the cosmological significance of these events for understanding the history of star formation in the universe.

6. We propose that the apparent break in the integrated counts of the EROs at $K \sim 19$–20 reflects the peak of the contribution from passive, evolved galaxies to this population. At magnitudes fainter than $K \sim 20$ we predict that the population will be increasingly dominated by dusty, active galaxies. The continuity in the properties of these faint dusty EROs connects them to samples of submillimeter-selected obscured starbursts at higher redshifts and fainter K-band magnitudes. This proposal can be tested by studies of the multiwavelength properties of extremely faint samples of EROs, $K \sim 23$, and their relationship to the blank-field populations of radio sources.

7. By identifying the likely contribution from dusty EROs to the total ERO population we estimate that the volume density of passive, evolved galaxies brighter than $K \leq 20.5$ is $\gtrsim 4 \times 10^{-4}$ Mpc^{-3}. Recent results point to a morphological diversity in the passive ERO population,

which would suggest that these galaxies should not be simply viewed as passively evolving ellipticals (Smith et al. 2002a). We conclude that previously well-fitting pure luminosity evolution models, which described the number counts of the whole ERO sample as due to a passively evolving elliptical population formed at high redshifts, will probably overpredict the number of truly passive EROs, and hence there is scope for the recent (trans)formation of some local elliptical galaxies. Nevertheless, the presence of luminous, passive galaxies at $z \sim 1$ does point to a phase of massive spheroid formation at higher redshifts, consistent with the interpretation of the SCUBA population as the formation phase of massive protoellipticals (Lilly et al. 1999; Smail et al. 2002a, 2002b). The typical, reddening-corrected luminosities of the radio-detected ERO population at $z \sim 1$ suggest that these galaxies will evolve into sub-L^* systems by the present day unless their star formation activity continues at a high rate for $\gg 10^8$ yr.

The area analyzed in this work covers a small fraction of the sensitive field of our VLA map; we expect to be able to quadruple the ERO sample available for analysis in the near future. In addition, we are undertaking a full photometric analysis of the ~1500 optically bright microjansky radio sources in this field using our panoramic *UBVRIzJHK* imaging data set (F. N. Owen et al. 2002, in preparation), constrained by deep spectroscopy from GMOS on Gemini.

We thank Taddy Kodama, F. Nakata, and S. Okamura for kindly allowing us to use their exquisite Subaru Suprime-Cam imaging. We also acknowledge useful conversations with Andrew Blain, Scott Chapman, Andrea Cimatti, Adriano Fontana, Bianca Poggianti, Alice Shapley, Graham Smith, and Chuck Steidel. We thank an anonymous referee for their thorough and constructive comments, which improved the clarity and presentation of this work. I. R. S. acknowledges support from a Royal Society University Research Fellowship and a Philip Leverhulme Prize Fellowship. G. E. M. gratefully acknowledges the support of JPL (contracts 1147 and 1166) and also the support of Vanguard Research, Inc.

REFERENCES

Aguerri, J. A. L., & Trujillo, I. 2002, MNRAS, 333, 633
Alexander, D. M., Brandt, W. N., Hornschemeier, A. E., Garmire, G. P., Schneider, D. P., Bauer, F. E., & Griffiths, R. E. 2001, AJ, 122, 2156
Alexander, D. M., Vignali, C., Bauer, F. E., Brandt, W. N., Hornschemeier, A. E., Garmire, G. P., & Schneider, D. P. 2002, AJ, 123, 1149
Barger, A. J., Cowie, L. L., & Richards, E. 2000, AJ, 119, 2092
Benn, C. R., Rowan-Robinson, M., McMahon, R., Broadhurst, T. J., & Lawrence, A. 1993, MNRAS, 263, 98
Bertin, E., & Arnouts, S. 1996, A&AS, 117, 393
Blain, A. W., Kneib, J.-P., Ivison, R. J., & Smail, I. 1999a, ApJ, 512, L87
Blain, A. W., Smail, I., Ivison, R. J., & Kneib, J.-P. 1999b, MNRAS, 302, 632
Bolzonella, M., Miralles, J.-M., & Pelló, R. 2000, A&A, 363, 476
Brusa, M., Comastri, A., Daddi, E., Cimatti, A., & Vignali, C. 2002, in X-Ray Spectroscopy of AGN with *Chandra* and *XMM/Newton*, ed. Th. Boller, S. Komossa, S. Kahn, & H. Kunioda (Garching: MPE), in press
Calzetti, D., et al. 2000, ApJ, 533, 682
Carilli, C. L., & Yun, M. S. 2000, ApJ, 530, 618
Carilli, C. L., et al. 2002, ApJ, submitted
Chapman, S. C., Blain, A. W., Ivison, R. J., & Smail, I. 2002a, Nature, submitted
Chapman, S. C., McCarthy, P. J., & Persson, S. E. 2000, AJ, 120, 1612
Chapman, S. C., Richards, E. A., Lewis, G., Wilson, G., & Barger, A. 2001, ApJ, 548, L147
Chapman, S. C., et al. 2002b, ApJ, submitted
Chen, H.-W., et al. 2002, ApJ, 570, 54
Cimatti, A., et al. 2002, A&A, 381, L68
Cole, S., Lacey, C. G., Baugh, C. M., & Frenk, C. S. 2000, MNRAS, 319, 168
Cole, S., et al. 2001, MNRAS, 326, 255
Condon, J. J. 1992, ARA&A, 30, 575
Condon, J. J., Anderson, M. L., & Helou, G. 1991, ApJ, 376, 95
Connolly, A., Szalay, A. S., Dickinson, M., Subbarao, M. U., & Brunner, R. J. 1997, ApJ, 486, L11
Cowie, L. L., Barger, A. J., & Kneib, J.-P. 2002, AJ, 123, 2197
Cowie, L. L., et al. 2001, ApJ, 551, L9
Cram, L., Hopkins, A., Mobasher, B., & Rowan-Robinson, M. 1998, ApJ, 507, 155
Daddi, E., Broadhurst, T. J., Zamorani, G., Cimatti, A., Röttgering, H., & Renzini, A. 2001, A&A, 376, 825
Daddi, E., Cimatti, A., Pozzetti, L., Hoekstra, H., Röttgering, H. J. A., Renzini, A., Zamorani, G., & Mannucci, F. 2000, A&A, 361, 535
Daddi, E., et al. 2002, A&A, 384, L1
Dey, A., Graham, J. R., Ivison, R. J., Smail, I., Wright, G. S., & Liu, M. C. 1999, ApJ, 519, 610
Dressler, A., Oemler, A., Sparks, W. B., & Lucas, R. A. 1994, ApJ, 430, 107
Dressler, A., et al. 1997, ApJ, 490, 577
Firth, A. E., et al. 2002, MNRAS, 332, 617
Flores, H., et al. 1999, ApJ, 517, 148
Franceschini, A., Fadda, D., Cesarsky, C., Elbaz, D., Flores, H., & Granato, G. L. 2002, ApJ, 568, 470
Gallego, J., Zamorano, J., Rego, M., & Vitores, A. G. 1997, ApJ, 475, 502
Gallimore, J. F., & Keel, W. C. 1993, AJ, 106, 1337
Gal-Yam, A., Ofek, E. O., Filippenko, A. V., Chornock, R., & Li, W. 2002, PASP, 114, 587
Gardner, J. P., Cowie, L. L., & Wainscoat, R. J. 1993, ApJ, 415, L9
Garrett, M. A. 2002, A&A, 384, L19
Georgakakis, A. E., Mobasher, B., Cram, L., & Hopkins, A. 1999, MNRAS, 310, L15
Giavalisco, M., & Dickinson, M. 2001, ApJ, 550, 177
Goldader, J. D., Meurer, G., Heckman, T. M., Seibert, M., Sanders, D. B., Calzetti, D., & Steidel, C. C. 2002, ApJ, 568, 651
Haarsma, D. B., Partridge, R. B., Windhorst, R. A., & Richards, E. A. 2000, ApJ, 544, 641
Hammer, F., Crampton, D., Lilly, S. J., Le Fevre, O., & Kenet, T. 1995, MNRAS, 276, 1085
Hauser, M. G., et al. 1998, ApJ, 508, 25
Hawarden, T. G., Leggett, S. K., Letawsky, M. B., Ballantyne, D. R., & Casali, M. M. 2001, MNRAS, 325, 563
Hopkins, A., Connolly, A. J., Haarsma, D. B., & Cram, L. E. 2001, AJ, 122, 288
Ivison, R. J., et al. 2002, MNRAS, in press
Iye, M., et al. 2000, PASJ, 52, 9
Kodama, T., Smail, I., Nakata, F., Okamura, S., & Bower, R. G. 2001, ApJ, 562, L9
Lagache, G., & Puget, J. L. 2000, A&A, 355, 17
Ledlow, M., Smail, I., Owen, F. N., Keel, W. C., Ivison, R. J., & Morrison, G. 2002, ApJ, 577, L79
Lilly, S. J., Tresse, L., Hammer, F., Crampton, D., & Le Fevre, O. 1995, ApJ, 455, 108
Lilly, S. J., et al. 1999, ApJ, 518, 641
Lutz, D., et al. 2001, A&A, 378, 70
Mainieri, V., et al. 2002, A&A, 393, 425
Mannucci, F., et al. 2002, MNRAS, 329, L57
Martini, P. 2001, AJ, 121, 598
McCarthy, P. J., et al. 2001, ApJ, 560, L131
Mirabel, I. F., & Sanders, D. B. 1989, ApJ, 340, L53
Mobasher, B., Cram, L., Georgakakis, A., & Hopkins, A. 1999, MNRAS, 308, 45
Mohan, N. R., Cimatti, A., Röttgering, H. J. A., Andreani, P., Severgnini, P., Tilanus, R. P. J., Carilli, C. L., & Stanford, S. A. 2002, A&A, 383, 440
Moran, E. C., Lehnert, M. D., & Helfand, D. J. 1999, ApJ, 526, 649
Moriondo, G., Cimatti, A., & Daddi, E. 2000, A&A, 364, 26
Morrison, G. E. 1999, Ph.D. thesis, Univ. New Mexico
Muxlow, T. W. B., et al. 1999, NewA Rev., 43, 623
Packham, C., et al. 2002, MNRAS, submitted
Page, M. J., Stevens, J. A., Mittaz, J. P. D., & Carrera, F. J. 2002, Science, 294, 2516
Persson, S. E., McCarthy, P., Dressler, A., & Matthews, K. 1993, in The Evolution of Galaixes and Their Environments, NASA Tech. Report, ed. M. Shull & H. Thronson (Washington, DC: GPO), 78
Pierre, M., et al. 2001, A&A, 372, L45
Poggianti, B. M., & Wu, H. 2000, ApJ, 529, 157
Pozzetti, L., & Mannucci, F. 2000, MNRAS, 317, L17
Ranalli, P., Comastri, A., & Setti, G. 2002, in New Visions of the X-Ray Universe, ed. F. Jansen (ESA SP-488; Noordwijk: ESA), in press
Richards, E. A. 1998, Ph.D. thesis, Univ. Virginia

Richards, E. A. 1999, ApJ, 513, L9
———. 2000, ApJ, 533, 611
Richards, E. A., Fomalont, E. B., Kellermann, K. I., Windhorst, R. A., Partridge, R. B., Cowie, L. L., & Barger, A. J. 1999, ApJ, 526, L73
Richards, E. A., Kellermann, K. I., Fomalont, E. B., Windhorst, R. A., & Partridge, R. B. 1998, AJ, 116, 1039
Roche, N., Almaini, O., Dunlop, J. S., Ivison, R. J., & Willott, C. 2002a, MNRAS, submitted
Roche, N., Lowenthal, J., & Koo, D. 2002b, MNRAS, 330, 307
Sanders, D. B., & Mirabel, I. F. 1996, ARA&A, 34, 749
Schindler, S., Belloni, P., Ikebe, Y., Hattori, M., Wambsganss, J., & Tanaka, Y. 1998, A&A, 338, 843
Seitz, C., Kneib, J.-P., Schneider, P., & Seitz, S. 1996, A&A, 314, 707
Serjeant, S., Gruppioni, C., & Oliver, S. 2002, MNRAS, 330, 621
Serjeant, S., Mobasher, B., Gruppioni, C., & Oliver, S. 2000, MNRAS, 317, L29
Smail, I., Ivison, R. J., Blain, A. W., & Kneib, J.-P. 2002a, MNRAS, 331, 495
Smail, I., Ivison, R. J., Gilbank, D. G., Dunlop, J. S., Keel, W. C., & Stevens, J. A. 2002b, ApJL, in press
Smail, I., Ivison, R. J., Kneib, J.-P., Cowie, L. L., Blain, A. W., Barger, A. J., Owen, F. N., & Morrison, G. 1999a, MNRAS, 308, 1061
Smail, I., Morrison, G., Gray, M. E., Owen, F. N., Ivison, R. J., Kneib, J.-P., & Ellis, R. S. 1999b, ApJ, 525, 609
Smith, G. P., Smail, I., Kneib, J.-P., Davis, C. J., Takamiya, M., Ebeling, H., & Czoske, O. 2002a, MNRAS, 333, L16
Smith, G. P., Treu, T., Ellis, R. S., Smail, I., Kneib, J.-P., & Frye, B. L. 2001, ApJ, 562, 635
Smith, G. P., et al. 2002b, MNRAS, 330, 1
Snigula, J., Drory, N., Bender, R., Botzler, C. S., Feulner, G., & Hopp, U. 2002, MNRAS, in press
Soifer, B. T., Matthews, K., Neugebauer, G., Armus, L., Cohen, J. G., Persson, S. E., & Smail, I. 1999, AJ, 118, 2065
Stanford, S. A., Eisenhardt, P. R. M., & Dickinson, M. 1995, ApJ, 450, 512
Stevens, J. A., Page, M. J., Ivison, R. J., Smail, I., Lehmann, I., Hassinger, G., & Szokoly, G. 2002, MNRAS, submitted
Thompson, D., et al. 1999, ApJ, 523, 100
Trager, S. C., Faber, S. M., Dressler, A., & Oemler, A. 1997, ApJ, 485, 92
Trentham, N., Kormendy, J., & Sanders, D. 1999, AJ, 117, 2152
Waddington, I., Windhorst, R. A., Cohen, S. H., Partridge, R. B., Spinrad, H., & Stern, D. 1999, ApJ, 526, L77
Waddington, I., Windhorst, R. A., Dunlop, J. S., Koo, D. C., & Peacock, J. A. 2000, MNRAS, 317, 801
Willott, C. J., Rawlings, S., & Blundell, K. M. 2001, MNRAS, 324, 1
Windhorst, R. A., Gordon, J. M., Pascarelle, S. M., Schmidtke, P. C., Keel, W. C., Burkey, J. M., & Dunlop, J. S. 1994, ApJ, 435, 577
Yan, L. 2001, in ASP Conf. Ser. 240, Gas and Galaxy Evolution, ed. J. E. Hibbard, M. P. Rupen, & J. H. van Gorkom (San Francisco: ASP), 117
Yan, L., McCarthy, P. J., Freudling, W., Teplitz, H. I., Malumuth, E. M., Weymann, R. J., & Malkan, M. A. 1999, ApJ, 519, L47
Yun, M. S., Reddy, N. A., & Condon, J. J. 2001, ApJ, 554, 803